Regional chronostratigraphy in the eastern Lesser Antilles quaternary fore-arc and accretionary wedge sediments: Relative paleointensity, oxygen isotopes and reversals

Arthur Bieber, Guillaume St-Onge, Nathalie Feuillet, J. Carlut, Elisabeth Michel, Eva Moreno

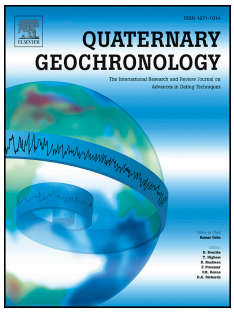

Regional chronostratigraphy in the eastern Lesser Antilles quaternary fore-arc and accretionary wedge sediments: Relative paleointensity, oxygen isotopes and reversals

A. Bieber, G. St-Onge, N. Feuillet, J. Carlut, E. Moreno, E. Michel

PII: S1871-1014(21)00030-3

DOI: https://doi.org/10.1016/j.quageo.2021.101179

Reference: QUAGEO 101179

To appear in: *Quaternary Geochronology*

Received Date: 27 July 2020

Revised Date: 28 February 2021

Accepted Date: 5 April 2021

Please cite this article as: Bieber, A., St-Onge, G., Feuillet, N., Carlut, J., Moreno, E., Michel, E., Regional chronostratigraphy in the eastern Lesser Antilles quaternary fore-arc and accretionary wedge sediments: Relative paleointensity, oxygen isotopes and reversals, *Quaternary Geochronology* (2021), doi: https://doi.org/10.1016/j.quageo.2021.101179.

accretionary wedge sediments: relative paleointensity, oxygen isotopes and reversals

Bieber, A.[1,2,*], St-Onge, G.[1], Feuillet, N.[2], Carlut, J.[2], Moreno, E.[3], Michel, E[4].

[1]Institut des sciences de la mer de Rimouski (ISMER), Canada Research Chair in Marine Geology, Université du Québec à Rimouski (UQAR) and GEOTOP, Rimouski (Québec), Canada

[2]Institut de physique du globe de Paris (IPGP), Université Sorbonne Paris Cité, Paris, France

[3]Laboratoire d'Océanographie et du Climat (LOCEAN), Sorbonne Université/CNRS/IRD/MNHN, Paris, France

[4]Laboratoire des Sciences du Climat et de l'Environnement, Bât 714, L'Orme des Merisiers, 91190 Gif-sur-Yvette, France

*Corresponding author:

E-mail address: arthur.bieber.ab@gmail.com (A. Bieber)

Abstract

Paleomagnetism is a powerful tool for establishing an almost continuous chronostratigraphy for an entire region. When combined with other dating methods, absolute or relative, it can be used to develop a regional reference chronostratigraphic framework. During the summer of 2016, several piston cores were collected along the Atlantic side of the Lesser Antilles onboard the R/V *Pourquoi pas?* as part of the CASEIS Expedition. Core CAS16-24PC was devoted to chronostratigraphic analysis and allowed development of a quasi-continuous Quaternary record.

layers, we reconstructed the relative paleointensity (RPI) variations by normalizing the natural remanent magnetization with the laboratory induced anhysteretic remanent magnetization. An age model was developed by comparing our RPI record with the PISO-1500 stack and paleomagnetic axial dipole moment model for the past 2 Myr (PADM-2M) and the planktic oxygen isotopic record ($\delta^{18}O$) for core CAS16-24PC with the LR04 benthic stack. By combining the $\delta^{18}O$ stratigraphy with paleomagnetic analyses, we established an age model covering the Brunhes/Matuyama boundary and Jaramillo Subchron back to ~1.15 Ma with a mean sedimentation rate of 1.7 cm/kyr. This age model complements the paleomagnetic data from IODP campaigns and volcanic records, and offers almost complete inclination, declination and RPI records as a local reference.

Keywords: Lesser Antilles, Quaternary, sediment, geomagnetic reversals, relative paleointensity, oxygen isotopes

1 Introduction

Earth's magnetic field varies at different timescales and can undergo reversals (normal and reverse polarities) that may be globally recorded quasi-simultaneously in rocks and sediments (Lowrie, 2007). The synchronicity of reversals across different locations makes them important for stratigraphy (Hambach et al., 2008). The last reversal occurred 773 ± 2 ka ago between the normal polarity Brunhes Chron and the reversed polarity Matuyama Chron (Singer, 2014; Simon et al. 2019; Channell et al., 2020). The Matuyama/Brunhes boundary (MBB) delimits the beginning of the Middle Pleistocene (International Commission on Stratigraphy, 2020). In

in Earth's magnetic field intensity. Full vector analysis of Quaternary oceanic sediment cores enables quasi-continuous reconstruction of the relative variations in the Earth's magnetic field (e.g., Tauxe, 1993; Weeks et al. 1993; Stoner and St-Onge, 2007; Channell et al., 2012, 2014, 2019; Roberts et al., 2013; Liu et al. 2016; Deschamps et al. 2018; Simon et al. 2020). This reconstruction is based on the assumption that magnetic minerals such as magnetite and titano-magnetite within the sediment reflect the strength and the direction of the Earth magnetic field at the time they were deposited. This non-destructive approach enables correlation of multiple cores and stratigraphic events for entire regions. While paleomagnetism has been widely used to understand past geomagnetic field fluctuations, increasing global data coverage remains a long-term challenge for understanding geomagnetic field dynamics (Korte and Mandea, 2019), and for chronostratigraphic purposes.

There is currently no complete and well-dated Quaternary magnetostratigraphic record for the Lesser Antilles. Most paleomagnetic studies have focused on volcanic rocks (Carlut and Quidelleur, 2000; Genevey et al., 2002; Tanty et al., 2015; Ricci et al., 2018) or Ocean Drilling Program (ODP) cores that cover longer geologic time intervals (DSDP Site 502: Kent and Spariosu, 1983; DSDP Leg 78A: Wilson, 1984; ODP Leg 110: Hounslow et al., 1990), but with a less detailed representation of the Quaternary.

The main objective of this study is to establish a complete regional Quaternary chronostratigraphy based on analyses of core CAS16-24PC retrieved during the CASEIS expedition (May 28 to July 4, 2016; Feuillet, 2016) onboard the R/V *Pourquoi Pas?*. The first step was to identify all rapidly deposited layers (RDL) using x-ray fluorescence, and physical and magnetic parameters to create a continuous composite record. The second step was to reconstruct a reliable relative paleointensity (RPI) record and to combine it to reversals and stable oxygen

71 Antilles.

72

The Lesser Antilles are located in the easternmost Caribbean Sea (Fig. 1). They are composed of two volcanic arcs: the inactive early Eocene to Oligocene arc and the current arc that has been active since 38 Ma (Briden et al., 1979; Bouysse and Westercamp, 1990). These arcs resulted from subduction of the south and north Atlantic oceanic crust under Caribbean oceanic crust (McDonald et al., 2000), which led to formation of basaltic volcanic arcs. The current average convergence velocity is 2 cm/yr with a NNE and SSW orientation (DeMets et al., 2000; Symithe et al., 2015). The current system is the product of a western arc migration following subduction of the two aseismic ridges (i.e., Tiburon and St-Luce) beneath the Caribbean plate. The volcanic activity is probably also related to the seismic activity (Davies, 1999; Leclerc et al., 2016). Seismic fault activation or reactivation led to two periods of maximum eruptive activity during the Eocene-Oligocene and the late Miocene-early Pliocene (Bouysse and Westercamp, 1990).

The Lesser Antilles arc basement has an asymmetric shape (Picard et al., 2006). Westward of the island arc, the Grenada back-arc basin has a steep and narrow continental shelf. In contrast, eastward of the island arc, the shelf is wider and limited eastwards by the accretionary wedge and the trench. The insular shelf is 250 km wide in the south, and only 80-100 km wide in the north. Similarly, the accretionary prism has a width of 300 km in the south that decreases northward to 50 km. The trench is deeper to the north (up to 8 km below sea-level). The sedimentary fill consists of (1) shallow shelf sediment predominantly composed (up to 50 %) of river discharge volcaniclastic sediments (the proportion increases closer to islands shore, up to 50 %) and pelagic and hemipelagic carbonate sediments, (2) deep sea sediments mostly composed of pelagic, hemipelagic and remobilized carbonates, and (3) volcaniclastic turbidite and tephra deposits (Reid et al., 1996; Picard et al., 2006). However, the most important terrigenous sediment sources

97 contribution from aeolian dust from Africa (Reid et al., 1996; Picard et al., 2006).

98 **3 Material and methods**

99 A bathymetric map (Fig. 1) was created with the QGIS software using the General Bathymetric
100 Chart of the Oceans GEBCO_08 grid, version 20100927 (http://www.gebco.net) and Digital
101 Elevation Models from the 2016 CASEIS cruise (Feuillet, 2016; Seibert et al., 2020). A 100-m
102 resolution was used with a WGS84/UTM World Mercator (15.5°N) projection. Reference core
103 CAS16-24PC (Fig. 1) was retrieved during the CASEIS expedition at 4023 m depth with a
104 Calypso piston corer on board the R/V *Pourquoi Pas?* (IFREMER fleet). The core is stored in the
105 marine collection of the *Muséum national d'Histoire naturelle* (Paris, France) under the number
106 MNHN-GS-CAS16-24PC and is 19.90 m in length and was divided into fourteen 150 cm
107 sections labeled with Roman numbers I to XIV (Fig. 2-A). Each section was measured on board
108 with a Multi Sensor Core Logger (see below), then split, photographed, described and sampled
109 with u-channels (u-shaped plastic tubes with 2 x 2 cm cross-section and up to 150 cm in length)
110 for continuous paleomagnetic analysis (e.g., Weeks et al., 1993; Stoner and St-Onge, 2007). In
111 2018, the core was sampled with plastic cubes (1.9 x 1.9 x 1.9 cm) for discrete paleomagnetic
112 analyses.

113 **3.1 Multi Sensor Core Logger analysis, CT scanning and x-ray fluorescence**

114 The GEOTEK Multi Sensor Core Logger (MSCL) from ISMER (*Institut des sciences de la mer*
115 *de Rimouski)* was used on board during the expedition to measure the physical and magnetic
116 properties of the sediments (St-Onge et al., 2007). Bulk density (obtained with gamma ray
117 attenuation), P-wave velocities and volumetric magnetic susceptibility (k) were analysed at 1-cm
118 intervals on whole core sections. After splitting the core, archive halves were photographed with

Instruments MS2E1 point sensor for magnetic susceptibility. Diffuse spectral reflectance data were also measured at 1-cm intervals using a Minolta CM-2600d spectrophotometer inline with the MSCL. Data were converted into the L*a*b* colour space of the International Commission on Illumination (CIE): L* ranges from black (0) to white (100), a* ranges from green (-60) to red (+60), and b* ranges from blue (-60) to yellow (+60). U-channel samples were scanned at *the Institut national de recherche scientifique – Centre eau, terre et environnement* (INRS-ETE, Québec, Canada) with a CT scanner. The resulting digital X-ray images were displayed in greyscale and expressed as CT numbers, which primarily reflect bulk density changes (e.g., St-Onge et al., 2007; Fortin et al., 2013). Major elements from Al to Ba were analysed on archive halves at the UMR CNRS 5805 EPOC laboratory (Bordeaux, France) using an X-Ray fluorescence (XRF) Avaatech core-scanner. XRF-measurements were conducted at 1 cm intervals with two tube voltages (10 and 30 keV).

3.2 Paleomagnetic analysis

3.2.1 *Continuous magnetic measurements*

Continuous paleomagnetic data were acquired at 1-cm intervals on u-channel samples using a 2G Enterprises 755SRM-1.65 cryogenic magnetometer at the ISMER. The natural remanent magnetization (NRM) was first measured directly and then stepwise demagnetized and measured after each of 17 alternating field (AF) demagnetization steps (0 to 80 mT, 5 mT increments) until the residual magnetization was less than 15% of the initial magnetization. An anhysteretic remanent magnetization (ARM) was then induced using a 100 mT peak AF and a 50 µT direct current (DC) bias field. The ARM was measured following the same procedure and increment steps as the NRM. Finally, an isothermal remanent magnetization (IRM) and a saturation IRM (SIRM) were induced in DC fields of 0.3 T and 0.95 T, respectively, using a pulse magnetizer,

increments) and 4 steps for SIRM (0, 10, 30, 50 mT). The data were processed with the Excel spreadsheet developed by Mazaud (2005), which provided the paleomagnetic inclination, declination and the associated maximum angular deviation (MAD) values calculated for the characteristic remanent magnetization (ChRM; 10 to 40 mT steps). The pseudo S-ratio was determined using the $IRM_{0\ mT}$ induced at 300 mT divided by $SIRM_{0\ mT}$ induced at 950 mT (IRM/SIRM). This pseudoS-ratio, alike the classical S-ratio, is an indicator of the magnetic coercivity and mineralogy (St-Onge et al., 2003). Values close to 1 (IRM ≈ SIRM) indicate the preponderance of low coercivity minerals, whereas lower values are the expression of higher coercivity minerals (IRM < SIRM). The sediments from core CAS16-24PC are characterized by high values of IRM and SIRM (average value of all data >11 Am^{-1}) and the intensity of the SIRM is sometimes slightly lower than the IRM, leading to values of the pseudo-S ratio slightly higher than 1 in specific intervals. This is most likely due to the difficulty of the cryogenic magnetometer to perform precise measurements near the dynamic range of the instrument (Roberts, 2006). As a consequence, it prevents us from using the pseudo S-ratio lonely and continuously downcore, but we still use the average value in hemipelagic facies in conjunction with the other magnetic and imaging data (SEM, see below) to assess the magnetic mineralogy. Also, k_{ARM} is calculated by normalizing the ARM with the bias field value and is used as a magnetic grain size indicator (e.g., Banerjee et al., 1981; King et al., 1982).

3.2.2 *Discrete magnetic measurements*

To confirm and refine the continuous magnetic measurements results and to improve delimitation of suspected reversals, we measured paleomagnetic data on discrete samples. They were acquired at 40-cm intervals along the whole core except for the uppermost 5 m (10 cm intervals) and sections with suspected geomagnetic reversals (2 cm intervals). We used a 2G Enterprises

stepwise demagnetization (10 steps; 5, 10, 15, 20, 30, 40, 50, 60, 70 and 90 mT) of the NRM at the *Institut de Physique du Globe de Paris* (IPGP).

Twenty-five bulk samples were selected and measured using a Princeton Measurement Corporation vibrating sample magnetometer (VSM) at the IPGP to obtain hysteresis loops and derived magnetic parameters corrected for high field and mass: coercive force (H_c), remanent coercive force (H_{cr}), saturation magnetisation (M_s) and saturation remanence (M_{rs}). These data were used to estimate the relative magnetic-grain sizes domains (single domain, multidomain and vortex state; Roberts et al.; 2017) based on the Day plot (Day et al., 1977). Attention must be taken when considering these results. As Roberts et al. (2018) pointed out, the Day diagram indicates strict limits for magnetic domains, while these limits depend on multiple parameters (e.g. magnetic grain size, mineralogy, mixing, shape). Three samples with highest magnetic susceptibility values were measured using an AGICO KLY-3 Kappa bridge system to measure the low-field magnetic susceptibility (k_{LF}) at high-temperatures. k_{LF} was measured in a heating-cooling cycle between room temperature and 700°C in a natural atmosphere. These measurements enable determination of Curie temperatures (Hrouda, 1994; Dunlop and Özdemir, 2007).

3.2.3 *Scanning electron microscopy and energy-dispersive X-ray spectroscopy*

The magnetic mineral fraction of five samples was manually separated from bulk powdered sediments using magnets. Imaging and energy-dispersive X-ray spectroscopy (EDS) microanalysis were observed with a EVO MA10 Zeiss scanning electron microscope (SEM).

3.3 Stable isotopes

Nineteen specimens were sampled in RDL and were removed from this study. $\delta^{18}O$ was determined on 250-315 µm sized *Globigerinoides ruber* planktic foraminifera using a Dual Inlet GV isoprime mass spectrometer at the *Laboratoire des Sciences du Climat et de l'Environnement* (LSCE). The measurements are reported versus the Vienna Pee Dee Belemnite standard (VPDB) with NBS-19 standard at $\delta^{18}O$ = -2.20‰, with a mean external reproducibility (1σ) of carbonate standards of ±0.05‰. Measured NBS-18 $\delta^{18}O$ values are -23.27 ± 0.10‰ VPDB.

3.4 Age model

The chronology of the event-free core CAS16-24PC composite record is based on paleomagnetic reversals, RPI variations and the $\delta^{18}O$ stratigraphy (see below). In this study, the R software package Bacon 2.2 (Blaauw and Christen, 2011) was used to produce a best-fit age model using Bayesian statistics with normal distributions. The parameters used were a 5 cm depth interval (d.by=10) and a 2 cm/ka mean accumulation rate (acc.mean=500).

4 Results

4.1 Morpho-bathymetry offshore of eastern Martinique

Core CAS16-24PC was retrieved offshore of Martinique Island at the limit between forearc and accretionary wedge sediments (Fig. 1). This limit follows approximately the local minimum negative gravity anomaly (dotted black line in Fig. 1), while the deformation front (white dashed line in Fig. 1) follows the outer prism limit (Westbrook et al., 1984; Bouysse and Westercamp, 1990). The core location is surrounded eastward by a deep basin down to 4400 m below sea level (mbsl) and westward by the Martinique basin deeper down to 5100 mbsl. This basin is fed from the south by the St. Lucia, the Caravelle, the Amerique and the Kalanina canyons, together with one canyon stemming from the accretionary prism (Seibert et al., 2020). In a north-south transect,

wasting events and frequent turbidity currents. The core site was chosen to collect the best possible chronostratigraphic reference core from the area, with the presence of carbonates for $\delta^{18}O$ stratigraphy (above the carbonate compensation depth) and the least possible turbidites. Nonetheless, in this volcanic setting, thin volcanoclastic layers are expected (e.g. Reid et al., 1996; Picard et al., 2000; Le Friant et al., 2008).

4.2 Lithology and rapidly deposited layer (RDL) determination

High-definition photographic images of the 19.90 m long piston core are presented in Fig. 2-A and confirm the overall homogeneity of brownish to greyish sediment. The associated CT-scan images have low (dark grey) to medium (light grey) density with traces of bioturbation. This background sediment is interbedded with thinner, darker sediment layers with higher density (white color) that can be related to RDL. In addition to the visual core characterization, down-core variations of–physical and magnetic parameters, CT-number, ln (Fe/Ca) XRF ratios and sedimentological log established onboard are shown in Fig. 2-B. The same method used by Cassidy et al. (2014) was used to decipher hemipelagic background sediments from RDL. Hemipelagic sediments are identified by traces of bioturbation, fine grains (under silt size), and relatively low and stable physical and magnetic parameter values. The mean ± 2 standard deviation (σ) limits (whitened bands delimited by vertical red lines) of each parameter was calculated, which gives a 95% (2σ) confidence level to delimit hemipelagic background sediments along the core, which is consistent with the photographic and CT-scan images. Outside the red lines, positive spikes in density parameters (gamma density, P-wave velocity and CT-number) and magnetic susceptibility reflect the presence of coarser grains, as well as ln (Fe/Ca) positive spikes and L* negative spikes, which reflect darker minerals with higher iron contents. Based on this analysis, magnetic susceptibility and density are the best parameters to establish the

low density (density around 1.29 g/cm^3, CT-numbers between 600 and 1028 HU) and weaker magnetic susceptibility (between 20 to 150x10^{-5} SI). The second facies (e.g. Fig. 3-B) has a sharp contact, coarser basal sediments with high density (up to 1.7 g/cm^3), high CT-number (up to 1977 HU), P-wave velocity spikes (up to 1701 m/s) and high magnetic susceptibility (up to 966x10^{-5} SI). The last facies is composed of silt layers with thicknesses of a few cm (e.g. Fig. 3-A) interbedded with hemipelagic background sediments with similar physical and magnetic parameters as facies 2, but without distinctive sharp contacts and normal grading. Facies 2 can be interpreted as classical turbidites because of its sharp contact and normal grading (e.g., Bouma, 1964), while facies 3 can be inferred to reflect deposition from suspended particles during a weak turbidity current with a slight normal grading at the base. Along the entire 24PC core, a total of 37 distinctive RDL were identified. Their thicknesses vary between 1 cm and 30 cm with a mean thickness of about 6 cm and a 5 cm median value; they related mostly to cryptotephras and reworked volcaniclastic material.

4.3 Creation of an event-free composite record.

One part of the core, from 10.32 m to 12.01 m, presents a specific signal that is mostly not related to turbidite or mass movement deposits. This section has no high values of density indicators or P-wave velocities, but L* and the photography (section VII_{132cm} to IX_{1cm}) indicate darker sediments. The XRF ratio ln (Fe/Ca) has high values, which combined with magnetic susceptibility and negative L* spikes, could indicate the presence of cryptotephras and reworked volcaniclastic minerals (Cassidy et al., 2014). The average magnetic susceptibility is higher than the background mean + 2 standard deviations, which is the upper limit for the hemipelagic sediments. However, density parameters do not indicate coarsening grain size. This implies magnetic mineral concentration variation, but in the absence of evidence for the deposition of a

composite depth) of the piston core is composed of background hemipelagic sediments. The following results are presented for this event-free stratigraphy as a function of meters composite depth (MCD; Table S-1 for depth correspondence) and the magnetic mineralogy was analyzed only on these hemipelagic sediments.

SEM imaging and EDS of the magnetic mineral fraction (Fig. 4) enabled the identification of magnetic minerals and reveal grain sizes mostly below 5 µm. The elemental compositions of the analyzed grains are compiled in supplementary material Table S- 2 and reveal a matrix composed mostly of alumino-silicates (Sample 4) with magnetic particles mostly consisting of low-titanium iron oxides grains (TiFeOx, samples 2, 3 and 5) and a few high-titanium iron oxide grains (not shown here). These SEM investigations are in agreement with the VSM measurements where the shapes of hysteresis loops (Fig. 5-A) are characteristic of low-coercivity ferrimagnetic minerals like magnetite or titanomagnetite (Day et al., 1977; Tauxe et al. 1996). In addition, magnetic susceptibility was measured every 18 seconds over a heating-cooling cycle from room temperature to 700°C and back to room temperature (Fig. 5-B). The presence of different magnetic minerals is revealed. High temperature curves suggest the identification of the magnetite Curie temperature (Fig. 5-B) at around 580 °C (Dunlop and Özdemir, 2007). The small peak between 300 °C and 370 °C can be interpreted as Ti-rich titanomagnetite (Gilder and Legoff, 2005). Additionally, the pseudo S-ratio in hemipelagic sediments presents an average value of 0.96. This value is typical of low coercivity minerals such as magnetite (Stoner and St-Onge, 2007). While EDS measurements only reflect mineralogy of minerals bigger than 1 µm and might be different from remanence carriers, the VSM and magnetic susceptibility measurements were made on bulk sediment. These combined results demonstrate an overall magnetic mineralogy dominated by magnetite and titanomagnetite. Such a magnetic composition is typical of volcanic settings and was previously observed for example in the Tobago Basin, Southeast Caribbean (Frank et al., 2016).

4.5 Magnetic grain size and concentration

Day-plot (Day et al., 1977), derived from hysteresis parameters (Fig. 6-A), confirms the relative prevalence of magnetic grains in a vortex state. In the King plot, data for almost all samples from the composite core range around the empirical 0.2 µm line, and except for 3 samples, all are above the 5 µm empirical line (Fig. 6-B). Even though these absolute values should be treated with caution because they were derived from synthetic magnetite (King et al., 1982), they nonetheless suggest a relatively fine magnetic grain size. These results are supported by SEM images (Fig. 4) that reveal particle sizes smaller than or equal to 5 µm. This can explain that the $NRM_{20\ mT}$, $ARM_{20\ mT}$ and $IRM_{20\ mT}$ values vary by less than an order of magnitude along the core (Fig. 7), except from 9.24 to 10.90 MCD (10.32 m to 12.01 m) where the density parameters do not exhibit coarsening grain size, while magnetic concentration increases (Fig. 2-B). Furthermore, the k_{ARM}/k ratio (Fig. 7), which reflects magnetic grain size variations (Banerjee et al., 1981; King et al., 1982; Stoner and St-Onge, 2007), has an overall constant trend.

4.6 Magnetic remanence

Magnetic u-channel measurements are presented in Figs. 8 and 9. Within all the demagnetization steps, the NRM varies between $7.95*10^{-4}$ and $2.93*10^{-1}$ A/m, while induced magnetization ARM and IRM (SIRM) vary, respectively, between $1.52*10^{-4}$ and $8.1*10^{-1}$ A/m, and $1.32*10^{-1}$ and 5.29 A/m. From the top to 12.25 MCD, a strong and stable single-component NRM is isolated from 10 to 40 mT (7 demagnetization steps; Fig. 8) with a clear linear trend toward the origin of the orthogonal projection (Fig. 9-A and B). The viscous component is removed easily within the first 2 demagnetization steps. The mean MAD is 7° and the median is 5.6°, which are indicative of relatively good directional data. In addition, the inclination fluctuates around the expected inclination for the site latitude for a geocentric axial dipole (GAD = 28.28°) field. From 12.25 MCD to the bottom of the core, a stable single-component magnetization is isolated from 10 to

interpreted as reversals. While the MAD values are relatively higher below 12.25 MCD (mean and median values of 18° and 15.6°, respectively), the inclinations fluctuate around the GAD values for both polarities (Fig. 8). The declination variations also mirror the inclination changes. In addition, discrete samples are coherent with u-channel data and improve the delimitation of the reversal event at 12.78 MCD (blue dots in Fig. 8). Overall, piston core CAS16-24PC has strong and stable single-component NRMs carried by PSD magnetite or titanomagnetite grains. The event-free composite record thus fulfills the criteria required for relative paleointensity (RPI) determinations (Levi and Banerjee, 1976; Tauxe, 1993; Stoner and St-Onge, 2007).

4.7 Relative paleointensity (RPI)

To reconstruct RPI variations, the NRM needs to be cleaned from the influence of lithological variations by using a normalizer such as ARM, IRM or k (Tauxe, 1993). k can be affected by paramagnetic grains that do not contribute to remanent magnetisation (Forster et al., 1994; Brachfeld and Banerjee, 2000), so we will not use it as a normalizer in this study. Two methods were compared to identify the best normalizer. The most used is the ratio method (e.g. Channell et al., 1997; Channell, 1999; St-Onge et al. 2003; Deschamps et al., 2018), which was calculated here using the average of seven demagnetization steps (10 to 40 mT) of the NRM normalized by ARM or IRM at the same steps (10 to 40 mT). To evaluate the best normalizer, the normalized NRM is plotted against the normalizer and must reveal the lowest coefficient of determination (r^2). Neither normalized remanence proxy correlates with their normalizers, but the r^2 value is lower for ARM (0.028) than for IRM (0.13) (Fig. 10). The second method, based on the pseudo-Thellier method and recognised as the slope method (e.g. Tauxe et al., 1995; Channell, 2002; Snowball and Sandgren, 2004; Xuan and Channell, 2009), uses the slope between the NRM and the normalizer at different demagnetization steps. To evaluate the efficiency of a normalizer

normalization gives the same results as for the slope method, discrepancies exist for IRM between both normalization methods. Also, the median r value is 0.99 for ARM, while it is 0.98 for IRM. Considering these arguments, ARM is here considered as the best normalizer and we use the ratio method for normalization.

5 Discussion

5.1 $\delta^{18}O$ stratigraphy and paleomagnetic dating

Marine sediment cores usually have age models based on stratigraphic alignment of the depth-scale $\delta^{18}O$ record with an already dated reference $\delta^{18}O$ record. We establish a first age-model by matching the planktic $\delta^{18}O$ record of core CAS16-24PC with the benthic reference LR04 stack (Fig. 11), which is an average of 57 globally distributed benthic $\delta^{18}O$ records (Lisiecki and Raymo, 2005) using a graphic correlation technique with the Analyseries software (Paillard et al., 1996). This correlation assumes a linear sedimentation rate between 2 tie-points. A total of 37 tie points (Table 1) were used and have an excellent correlation (r^2 = 0.75). In a second stage, the age-model was refined using paleomagnetic results from core CAS16-24PC (Fig. 8). Inclination and declination variations indicate that core CAS16-24PC covers the Brunhes Chron and the end of the Matuyama Chron, including the Jaramillo Subchron. While the paleomagnetic measurements made on the u-channels were of sufficient quality to identify these reversals, discrete measurements on cubes made it possible to detect the positions of reversals more accurately, especially when sedimentation rates are below 10 cm/kyr (Philippe et al., 2018). Thus, the 3 first polarity transitions were deduced from u-channel and discrete samples. The normal polarity Jaramillo Subchron begins at around 1069 ± 12 ka at 16.32 MCD and ends at around 1001 ka ± 10 ka at 15.38 MCD (Singer, 2014). The Matuyama/Brunhes boundary (MBB), occurred at 773 ka (Channell et al., 2010; Singer, 2014, Simon et al., 2019), and is recorded at

the PISO-1500 paleointensity stack (Channell et al., 2009). The match between the two datasets (Fig. 12) is reasonable for the Brunhes Chron ($r^2 = 0.45$), while for the Matuyama Chron part it is weaker ($r^2 = 0.33$). To complement these results, we also match our RPI curve against the PADM2M model (Ziegler et al., 2011). Within the Brunhes Chron, two intervals are more difficult to match. The first is between 100 and 150 ka, while the second interval is between 300 and 500 ka. However, 37 tie points (Fig. 12, green and blue dots) were derived from these two correlations and are listed in Table 2 and error estimations are described in Fig. S-1. The discrepancies between the reference curves and Lesser Antilles RPI before the MBB are likely to be the result of the lower quality data, as illustrated by the demagnetization curves (Fig. 9-D) and high MAD values (Fig. 8). From 900 to 1151 ka, the lack of continuous data points does not permit use of the RPI record as a sole chronostratigraphic marker.

5.2 Final age model and paleomagnetic record

Quaternary sediments can contain numerous time constraints such as geomagnetic polarity reversals, geomagnetic excursions, $\delta^{18}O$ and RPI stratigraphy (Richards and Andersen, 2013). The combination of RPI and $\delta^{18}O$ stratigraphy has been used in several studies to establish a stronger age model than with RPI or $\delta^{18}O$ alone (e.g., Channell et al., 1997, 2009, 2012; Stoner and St-Onge, 2007; Xuan et al., 2016). Our age model (Fig. 13) was generated using 3 reversals, 37 tie points derived from the reconstructed RPI record and 37 tie points derived from the $\delta^{18}O$ stratigraphy. This age model has an age of ~1.15 Ma at the base of the core (17.33 MCD). The mean sedimentation rate varies around 1.67 cm/kyr, ranging from 1.70 cm/kyr during the Brunhes Chron and 1.58 cm/kyr during the Matuyama Chron. This change between the Matuyama and Brunhes Chrons might reflect change in the astronomical control of paleoclimate across the mid-Pleistocene transition (Schmieder et al., 2000). The sedimentation rate in this age-

presence of thicker RDL (> 5 cm), and fewer $\delta^{18}O$ and paleomagnetic tie points. Nonetheless, the low sedimentation rates are similar to published data from the accretionary prism sediments with Brunhes Chron sedimentation rates between 1 and 3 cm/kyr (Damuth, 1977; Reid et al., 1996) and they are slightly lower than the sedimentation rate reported at 3 km landward of the Barbados subduction deformation front DSDP Site 541 (Wright, 1984), which is about 5 cm/kyr for the Quaternary epoch. This age-depth model is validated by comparison of our data with the stacks mentioned above (Fig. 14).

Long sedimentary paleomagnetic records have been published in the equatorial to sub-equatorial Indian Ocean (e.g. Meynadier et al., 1994; Oda et al., 2000) and Pacific Ocean (e.g. Shackleton et al., 1990; Yamazaki and Oda, 2005), and in the North and South Atlantic Ocean (e.g. Haag, 2000; Stoner et al., 2003; Hofmann and Fabian, 2007). We establish here a new chronostratigraphy for the sub-equatorial Atlantic Ocean based on reconstruction of RPI, geomagnetic polarity reversals and $\delta^{18}O$ stratigraphy for the last ~1.15 Ma (Fig. 13). The low sedimentation rates prevent for detailed study of the MBB or the Jaramillo Subchron, but the composite record provides the first late Quaternary magnetostratigraphy (Fig. 14, red curve, and Fig. S-2) in this area and complements younger (Frank et al., 2016) and older (Wilson, 1984; Hounslow et al., 1990) records.

Our results make a new contribution to the global coverage of paleomagnetic data by adding a detailed and almost continuous late Quaternary paleomagnetic record from the Lesser Antilles subduction zone. The chronostratigraphy established here will be useful to correlate and date numerous cores from the CASEIS campaign from this area (Seibert et al., 2020), as well as to date the RDL triggered by earthquakes (e.g. seismo-turbidites, Heezen and Ewing, 1952) and tsunamis (e.g. turbidite-homogenite complexes, San Pedro et al., 2017) in these cores.

The combination of strong chronostratigraphic markers based on two magnetic reversals and indirect dating methods based on $\delta^{18}O$ and RPI correlation enable the construction of an age model for core CAS16-24PC. However, in spite of the quality of the chronology proposed, our study has three limitations. First, we did not use any absolute dating methods (such as radiometric or luminescence dating). Second, reference records used in our study already have their own limitations and uncertainties. For the benthic LR04 stack, the uncertainties are about 6 ka from 3 to 1 Ma and 4 ka for the last Ma (Lisiecki and Raymo, 2005). The PISO-1500 stack is comparable to LR04 (Channell et al., 2009), while the PADM2M age model has an estimated uncertainty of 5-10 ka (Ziegler et al., 2011). Third, low sedimentation rate can limit the resolution of the record. However, the mean sedimentation rate in core CAS16-24PC is 1.7 cm/kyr what is similar to cores MD97-2140 and MD97-2143 used in the construction of the PISO-1500 stack (Channel et al. 2009). Considering these three limitations, the uncertainty of the reconstructed RPI is estimated at 10 ka on continuous measurements. Some periods of time were not recorded (for example in core breaks or between the sections) and some tie-points were found at the limit of these hiatuses and imply a greater uncertainty.

6 Conclusions

Magnetic, physical and chemical properties of the sediments enable identification of rapidly deposited layers and makes it able to build an event-free 1.51 Ma composite record for core CAS16-24PC. This sediment acquired a natural remanent magnetization characterized by a strong, well-defined, stable single component magnetization carried by fine-grained magnetite and titanomagnetite. These results allow for reconstructing a reliable relative paleointensity record for the last 900 ka, including the Brunhes/Matuyama boundary. This geomagnetic reversal

also record the limits of the Jaramillo Subchron.

The $\delta^{18}O$ stratigraphy combined with the reconstructed relative paleointensity and 3 reversal events recorded in core CAS16-24PC allow establishment of an age-depth model for the last ~1.15 Ma. This age model will be used to investigate earthquakes and tsunami recurrence in Lesser Antilles forearc and accretionary wedge sediments. Finally, even though the reference core was selected to avoid the recording of rapidly deposited layers, we have established a rapid and non-destructive method to identify thin turbidites and tephra layers based on the combination of several magnetic, physical and geochemical properties.

Acknowledgments

We thank the captain, officers and crew of the R/V Pourquoi Pas?, and the scientific participants in the CASEIS Expedition for the quality of the acquired shipboard data. This work was supported by grants from the Natural Sciences and Engineering Research Council of Canada (NSERC) and the French National Research Agency (ANR-17-CE03-0006; DS01 – CARQUAKES). We also thank Quentin Beauvais, Lola Johannes and Marie-Pier St-Onge for their help in the laboratory. A. Bieber acknowledges scholarships from the Institut des sciences de la mer de Rimouski (ISMER) and Institut de physique du globe de Paris (IPGP).

Data availability: https://data.mendeley.com/datasets/wv2bzwc98p/draft?a=3f1a879d-218d-4a7a-9d2d-276cdf70d0ce (Reserved DOI: 10.17632/wv2bzwc98p.1)

Banerjee, S.K., King, J., Marvin, J., 1981. A rapid method for magnetic granulometry with applications to environmental studies. Geophys. Res. Lett. 8, 333–336. https://doi.org/10.1029/GL008i004p00333

Blaauw, M., Christen, J.A., 2011. Flexible paleoclimate age-depth models using an autoregressive gamma process. Bayesian Analysis 6, 457–474. https://doi.org/10.1214/11-BA618

Bouma, A.H., 1964. Turbidites, in: Developments in Sedimentology. Elsevier, pp. 247–256. https://doi.org/10.1016/S0070-4571(08)70967-1

Bouysse, P., Westercamp, D., 1990. Subduction of Atlantic aseismic ridges and Late Cenozoic evolution of the Lesser Antilles island arc. Tectonophysics 175, 349–355, 357–380.

Brachfeld, S.A., Banerjee, S.K., 2000. A new high-resolution geomagnetic relative paleointensity record for the North American Holocene: A comparison of sedimentary and absolute intensity data. Journal of Geophysical Research: Solid Earth 105, 821–834. https://doi.org/10.1029/1999JB900365

Briden, J.C., Rex, D.C., Faller, A.M., Tomblin, J.F., 1979. K-Ar Geochronology and Palaeomagnetism of Volcanic Rocks in the Lesser Antilles Island Arc. Philosophical Transactions of the Royal Society A: Mathematical, Physical and Engineering Sciences 291, 485–528. https://doi.org/10.1098/rsta.1979.0040

Carlut, J., Quidelleur, X., 2000. Absolute paleointensities recorded during the Brunhes chron at La Guadeloupe Island. Physics of the Earth and Planetary Interiors 120, 255–269.

Cassidy, M., Watt, S.F.L., Palmer, M.R., Trofimovs, J., Symons, W., Maclachlan, S.E., Stinton, A.J., 2014. Construction of volcanic records from marine sediment cores: A review and case study (Montserrat, West Indies). Earth-Science Reviews 138, 137–155. https://doi.org/10.1016/j.earscirev.2014.08.008

Drilling Program Sites 983 and 984 (Iceland Basin). Journal of Geophysical Research 107. https://doi.org/10.1029/2001JB000491

Channell, J.E.T., 1999. Geomagnetic paleointensity and directional secular variation at Ocean Drilling Program (ODP) Site 984 (Bjorn Drift) since 500 ka: Comparisons with ODP Site 983 (Gardar Drift). Journal of Geophysical Research: Solid Earth 104, 22937–22951. https://doi.org/10.1029/1999JB900223

Channell, J.E.T., Hodell, D.A., Curtis, J.H., 2012. ODP Site 1063 (Bermuda Rise) revisited: Oxygen isotopes, excursions and paleointensity in the Brunhes Chron: ODP SITE 1063 REVISITED. Geochemistry, Geophysics, Geosystems 13. https://doi.org/10.1029/2011GC003897

Channell, J.E.T., Hodell, D.A., Lehman, B., 1997. Relative geomagnetic paleointensity and δ18O at ODP Site 983 (Gardar Drift, North Atlantic) since 350 ka. Earth and Planetary Science Letters 153, 103–118. https://doi.org/10.1016/S0012-821X(97)00164-7

Channell, J.E.T., Hodell, D.A., Singer, B.S., Xuan, C., 2010. Reconciling astrochronological and $^{40}Ar/^{39}Ar$ ages for the Matuyama-Brunhes boundary and late Matuyama Chron: MATUYAMA-BRUNHES REVERSAL AGES. Geochemistry, Geophysics, Geosystems 11. https://doi.org/10.1029/2010GC003203

Channell, J.E.T., Singer, B.S., Jicha, B.R., 2020. Timing of Quaternary geomagnetic reversals and excursions in volcanic and sedimentary archives. Quaternary Science Reviews 228, 106114. https://doi.org/10.1016/j.quascirev.2019.106114

Channell, J.E.T., Wright, J.D., Mazaud, A., Stoner, J.S., 2014. Age through tandem correlation of Quaternary relative paleointensity (RPI) and oxygen isotope data at IODP Site U1306 (Eirik

https://doi.org/10.1016/j.quascirev.2014.01.022

Channell, J.E.T., Xuan, C., Hodell, D.A., 2009. Stacking paleointensity and oxygen isotope data for the last 1.5 Myr (PISO-1500). Earth and Planetary Science Letters 283, 14–23. https://doi.org/10.1016/j.epsl.2009.03.012

Channell, J.E.T., Xuan, C., Hodell, D.A., Crowhurst, S.J., Larter, R.D., 2019. Relative paleointensity (RPI) and age control in Quaternary sediment drifts off the Antarctic Peninsula. Quaternary Science Reviews 211, 17–33. https://doi.org/10.1016/j.quascirev.2019.03.006

Damuth, J.E., 1977. Late Quaternary sedimentation in the western equatorial Atlantic. Geological Society of America Bulletin 88, 695. https://doi.org/10.1130/0016-7606(1977)88<695:LQSITW>2.0.CO;2

Davies, J.H., 1999. The role of hydraulic fractures and intermediate-depth earthquakes in subduction-zone magmatism. Nature 398, 142–145. https://doi.org/10.1038/18202

Day, R., Fuller, M., Schmidt, V.A., 1977. Hysteresis properties of titanomagnetites: Grain-size and compositional dependence. Physics of the Earth and Planetary Interiors 13, 260–267. https://doi.org/10.1016/0031-9201(77)90108-X

DeMets, C., Jansma, P.E., Mattioli, G.S., Dixon, T.H., Farina, F., Bilham, R., Calais, E., Mann, P., 2000. GPS geodetic constraints on Caribbean-North America Plate Motion. Geophysical Research Letters 27, 437–440. https://doi.org/10.1029/1999GL005436

Deschamps, C.-E., St-Onge, G., Montero-Serrano, J.-C., Polyak, L., 2018. Chronostratigraphy and spatial distribution of magnetic sediments in the Chukchi and Beaufort seas since the last deglaciation. Boreas 47, 544–564. https://doi.org/10.1111/bor.12296

Carillo, C., Patriat, M., Pichot, T., Loubrieux, B., Granjeon, D., 2015. Tectonics and sedimentation interactions in the east Caribbean subduction zone: An overview from the Orinoco delta and the Barbados accretionary prism. Marine and Petroleum Geology 64, 76–103. https://doi.org/10.1016/j.marpetgeo.2014.12.015

Dunlop, D.J., Özdemir, Ö., 2007. Magnetizations in Rocks and Minerals, in: Treatise on Geophysics. Elsevier, pp. 277–336. https://doi.org/10.1016/B978-044452748-6.00093-6

Feuillet, N., 2016. CASEIS cruise, RV Pourquoi pas ? https://doi.org/10.17600/16001800

Forster, Th., Evans, M.E., Heller, F., 1994. The frequency dependence of low field susceptibility in loess sediments. Geophysical Journal International 118, 636–642. https://doi.org/10.1111/j.1365-246X.1994.tb03990.x

Fortin, D., Francus, P., Gebhardt, A.C., Hahn, A., Kliem, P., Lisé-Pronovost, A., Roychowdhury, R., Labrie, J., St-Onge, G., 2013. Destructive and non-destructive density determination: method comparison and evaluation from the Laguna Potrok Aike sedimentary record. Quaternary Science Reviews 71, 147–153. https://doi.org/10.1016/j.quascirev.2012.08.024

Frank, U., Nowaczyk, N.R., Frederichs, T., Korte, M., 2016. Paleo- and rock magnetic investigations on Late Quaternary sediments from low latitudes I: Geomagnetic paleosecular variation and relative paleointensity records from the Tobago Basin, Southeast Caribbean. Geophysical Journal International ggw481. https://doi.org/10.1093/gji/ggw481

Genevey, A., Gallet, Y., Boudon, G., 2002. Secular variation study from non-welded pyroclastic deposits from Montagne Pelée volcano, Martinique (West Indies). Earth and Planetary Science Letters 201, 369–382. https://doi.org/10.1016/S0012-821X(02)00713-6

using the reversible susceptibility method, in: Advances in High-Pressure Technology for Geophysical Applications. Elsevier, pp. 315–335. https://doi.org/10.1016/B978-044451979-5.50017-X

Haag, M., 2000. Reliability of relative palaeointensities of a sediment core with climatically-triggered strong magnetisation changes. Earth and Planetary Science Letters 180, 49–59. https://doi.org/10.1016/S0012-821X(00)00145-X

Hambach, U., Rolf, C., Schnepp, E., 2008. Magnetic dating of Quaternary sediments, volcanites and archaeological materials: an overview. https://doi.org/10.3285/eg.57.1-2.2

Heezen, B.C., Ewing, W.M., 1952. Turbidity currents and submarine slumps, and the 1929 Grand Banks [Newfoundland] earthquake. American Journal of Science 250, 849–873. https://doi.org/10.2475/ajs.250.12.849

Hofmann, D.I., Fabian, K., 2007. Rock magnetic properties and relative paleointensity stack for the last 300 ka based on a stratigraphic network from the subtropical and subantarctic South Atlantic. Earth and Planetary Science Letters 260, 297–312. https://doi.org/10.1016/j.epsl.2007.05.042

Hounslow, M.W., Bootes, P.A., Whyman, G., 1990. 25. Remanent magnetization of sediments undergoing deformation in the Barbados accretionary prism: ODP LEG110. https://doi.org/10.2973/odp.proc.sr.110.155.1990

Hrouda, F., 1994. A technique for the measurement of thermal changes of magnetic susceptibility of weakly magnetic rocks by the CS-2 apparatus and KLY-2 Kappabridge. Geophysical Journal International 118, 604–612. https://doi.org/10.1111/j.1365-246X.1994.tb03987.x

564 deep-sea sediments. Palaeogeography, Palaeoclimatology, Palaeoecology 42, 47–64.
565 https://doi.org/10.1016/0031-0182(83)90038-X

566 King, J., Banerjee, S.K., Marvin, J., Özdemir, Ö., 1982. A comparison of different magnetic methods
567 for determining the relative grain size of magnetite in natural materials: Some results from lake
568 sediments. Earth and Planetary Science Letters 59, 404–419. https://doi.org/10.1016/0012-
569 821X(82)90142-X

570 Korte, M., Mandea, M., 2019. Geomagnetism: From Alexander von Humboldt to Current Challenges.
571 Geochemistry, Geophysics, Geosystems 20, 3801–3820. https://doi.org/10.1029/2019GC008324

572 Le Friant, A., Lock, E.J., Hart, M.B., Boudon, G., Sparks, R.S.J., Leng, M.J., Smart, C.W.,
573 Komorowski, J.C., Deplus, C., Fisher, J.K., 2008. Late Pleistocene tephrochronology of marine
574 sediments adjacent to Montserrat, Lesser Antilles volcanic arc. Journal of the Geological Society
575 165, 279–289. https://doi.org/10.1144/0016-76492007-019

576 Leclerc, F., Feuillet, N., Deplus, C., 2016. Interactions between active faulting, volcanism, and
577 sedimentary processes at an island arc: Insights from Les Saintes channel, Lesser Antilles arc:
578 FAULTING, VOLCANISM, AND TURBIDITY SYSTEMS. Geochemistry, Geophysics,
579 Geosystems 17, 2781–2802. https://doi.org/10.1002/2016GC006337

580 Levi, S., Banerjee, S.K., 1976. On the possibility of obtaining relative paleointensities from lake
581 sediments. Earth and Planetary Science Letters 29, 219–226. https://doi.org/10.1016/0012-
582 821X(76)90042-X

583 Lisiecki, L.E., Raymo, M.E., 2005. A Pliocene-Pleistocene stack of 57 globally distributed benthic δ^{18}
584 O records: PLIOCENE-PLEISTOCENE BENTHIC STACK. Paleoceanography 20.
585 https://doi.org/10.1029/2004PA001071

587 Magnetostratigraphy of a long Quaternary sediment core in the South Yellow Sea. Quaternary
588 Science Reviews 144, 1–15. https://doi.org/10.1016/j.quascirev.2016.05.025

589 Lowrie, W., 2007. Magnetostratigraphy, in: Gubbins, D., Herrero-Bervera, E. (Eds.), Encyclopedia of
590 Geomagnetism and Paleomagnetism. Springer Netherlands, Dordrecht, pp. 664–670.
591 https://doi.org/10.1007/978-1-4020-4423-6_206

592 Macdonald, R., Hawkesworth, C.J., Heath, E., 2000. The Lesser Antilles volcanic chain: a study in arc
593 magmatism. Earth-Science Reviews 49, 1–76.

594 Meynadier, L., Valet, J.-P., Bassinot, F.C., Shackleton, N.J., Guyodo, Y., 1994. Asymmetrical saw-
595 tooth pattern of the geomagnetic field intensity from equatorial sediments in the Pacific and
596 Indian Oceans. Earth and Planetary Science Letters 126, 109–127. https://doi.org/10.1016/0012-
597 821X(94)90245-3

598 Oda, H., Shibuya, H., Hsu, V., 2000. Palaeomagnetic records of the Brunhes/Matuyama polarity
599 transition from ODP Leg 124 (Celebes and Sulu seas). Geophysical Journal International 142,
600 319–338. https://doi.org/10.1046/j.1365-246x.2000.00130.x

601 Paillard, D., Labeyrie, L., Yiou, P., 1996. Macintosh Program performs time-series analysis. Eos,
602 Transactions American Geophysical Union 77, 379–379. https://doi.org/10.1029/96EO00259

603 Philippe, É.G.H., Valet, J., St□Onge, G., Thevarasan, A., 2018. Are Paleomagnetic Records From U□
604 Channels Appropriate for Studies of Reversals and Excursions? Geochemistry, Geophysics,
605 Geosystems 19, 4130–4142. https://doi.org/10.1029/2018GC007803

margin: the Lesser Antilles arc system. Geo-Marine Letters 26, 397–410. https://doi.org/10.1007/s00367-006-0046-y

Reid, R.P., Carey, S.N., Ross, D.R., 1996. Late Quaternary sedimentation in the Lesser Antilles island arc. Geological Society of America Bulletin 108, 78–100. https://doi.org/10.1130/0016-7606(1996)108<0078:LQSITL>2.3.CO;2

Ricci, J., Carlut, J., Valet, J.-P., 2018. Paleosecular variation recorded by Quaternary lava flows from Guadeloupe Island. Scientific Reports 8. https://doi.org/10.1038/s41598-018-28384-z

Richards, D.A., Andersen, M.B., 2013. Time Constraints and Tie-Points in the Quaternary Period. Elements 9, 45–51. https://doi.org/10.2113/gselements.9.1.45

Roberts, A.P., 2006. High-resolution magnetic analysis of sediment cores: Strengths, limitations and strategies for maximizing the value of long-core magnetic data. Physics of the Earth and Planetary Interiors 156, 162–178. https://doi.org/10.1016/j.pepi.2005.03.021

Roberts, A.P., Almeida, T.P., Church, N.S., Harrison, R.J., Heslop, D., Li, Y., Li, J., Muxworthy, A.R., Williams, W., Zhao, X., 2017. Resolving the Origin of Pseudo-Single Domain Magnetic Behavior: Origin of PSD Behavior. J. Geophys. Res. Solid Earth 122, 9534–9558. https://doi.org/10.1002/2017JB014860

Roberts, A.P., Tauxe, L., Heslop, D., 2013. Magnetic paleointensity stratigraphy and high-resolution Quaternary geochronology: successes and future challenges. Quaternary Science Reviews 61, 1–16. https://doi.org/10.1016/j.quascirev.2012.10.036

Roberts, A.P., Tauxe, L., Heslop, D., Zhao, X., Jiang, Z., 2018. A Critical Appraisal of the “Day” Diagram. J. Geophys. Res. Solid Earth 123, 2618–2644. https://doi.org/10.1002/2017JB015247

Augias deposit in the Ionian Sea (Central Mediterranean Sea), based on new regional sedimentological data. Marine Geology 384, 199–213. https://doi.org/10.1016/j.margeo.2016.05.005

Schmieder, F., von Dobeneck, T., Bleil, U., 2000. The Mid-Pleistocene climate transition as documented in the deep South Atlantic Ocean: initiation, interim state and terminal event. Earth and Planetary Science Letters 179, 539–549. https://doi.org/10.1016/S0012-821X(00)00143-6

Seibert, C., Feuillet, N., Ratzov, G., Beck, C., Cattaneo, A., 2020. Seafloor morphology and sediments transfers in the mixed carbonated-siliciclastic environment of the Lesser Antilles forearc along Barbuda and St. Lucia. Marine Geology 106242. https://doi.org/10.1016/j.margeo.2020.106242

Shackleton, N.J., Berger, A., Peltier, W.R., 1990. An alternative astronomical calibration of the lower Pleistocene timescale based on ODP Site 677. Transactions of the Royal Society of Edinburgh: Earth Sciences 81, 251–261. https://doi.org/10.1017/S0263593300020782

Simon, Q., Ledru, M.-P., Sawakuchi, A.O., Favier, C., Mineli, T.D., Grohmann, C.H., Guedes, M., Bard, E., Thouveny, N., Garcia, M., Tachikawa, K., Rodríguez-Zorro, P.A., 2020. Chronostratigraphy of a 1.5±0.1 Ma composite sedimentary record from Colônia basin (SE Brazil): Bayesian modeling based on paleomagnetic, authigenic 10Be/9Be, radiocarbon and luminescence dating. Quaternary Geochronology 58, 101081. https://doi.org/10.1016/j.quageo.2020.101081

Simon, Q., Suganuma, Y., Okada, M., Haneda, Y., 2019. High-resolution 10Be and paleomagnetic recording of the last polarity reversal in the Chiba composite section: Age and dynamics of the Matuyama–Brunhes transition. Earth and Planetary Science Letters 519, 92–100. https://doi.org/10.1016/j.epsl.2019.05.004

29–52. https://doi.org/10.1016/j.quageo.2013.10.003

Snowball, I., Sandgren, P., 2004. Geomagnetic field intensity changes in Sweden between 9000 and 450 cal BP: extending the record of “archaeomagnetic jerks” by means of lake sediments and the pseudo-Thellier technique. Earth and Planetary Science Letters 227, 361–376. https://doi.org/10.1016/j.epsl.2004.09.017

Stoner, J.S., Channell, J.E.T., Hodell, D.A., Charles, C.D., 2003. A ~580 kyr paleomagnetic record from the sub-Antarctic South Atlantic (Ocean Drilling Program Site 1089): PALEOMAGNETIC RECORD FROM THE SOUTH ATLANTIC. Journal of Geophysical Research: Solid Earth 108. https://doi.org/10.1029/2001JB001390

Stoner, J.S., St-Onge, G., 2007. Chapter Three Magnetic Stratigraphy in Paleoceanography: Reversals, Excursions, Paleointensity, and Secular Variation, in: Developments in Marine Geology. Elsevier, pp. 99–138. https://doi.org/10.1016/S1572-5480(07)01008-1

St-Onge, G., Mulder, T., Francus, P., Long, B., 2007. Chapter Two Continuous Physical Properties of Cored Marine Sediments, in: Developments in Marine Geology. Elsevier, pp. 63–98. https://doi.org/10.1016/S1572-5480(07)01007-X

St-Onge, G., Stoner, J.S., Hillaire-Marcel, C., 2003. Holocene paleomagnetic records from the St. Lawrence Estuary, eastern Canada: centennial- to millennial-scale geomagnetic modulation of cosmogenic isotopes. Earth and Planetary Science Letters 209, 113–130. https://doi.org/10.1016/S0012-821X(03)00079-7

Symithe, S., Calais, E., de Chabalier, J.B., Robertson, R., Higgins, M., 2015. Current block motions and strain accumulation on active faults in the Caribbean: CURRENT CARIBBEAN

https://doi.org/10.1002/2014JB011779

Tanty, C., Carlut, J., Valet, J.-P., Germa, A., 2015. Palaeosecular variation recorded by 9 ka to 2.5-Ma-old lavas from Martinique Island: new evidence for the La Palma aborted reversal 617 ka ago. Geophysical Journal International 200, 915–932. https://doi.org/10.1093/gji/ggu423

Tauxe, L., 1993. Sedimentary records of relative paleointensity of the geomagnetic field: Theory and practice. Reviews of Geophysics 31, 319. https://doi.org/10.1029/93RG01771

Tauxe, L., Mullender, T.A.T., Pick, T., 1996. Potbellies, wasp-waists, and superparamagnetism in magnetic hysteresis. Journal of Geophysical Research: Solid Earth 101, 571–583. https://doi.org/10.1029/95JB03041

Tauxe, L., Pick, T., Kok, Y.S., 1995. Relative paleointensity in sediments: A Pseudo-Thellier Approach. Geophysical Research Letters 22, 2885–2888. https://doi.org/10.1029/95GL03166

Weeks, R., Laj, C., Endignoux, L., Fuller, M., Roberts, A., Manganne, R., Blanchard, E., Goree, W., 1993. Improvements in long-core measurement techniques: applications in palaeomagnetism and palaeoceanography. Geophysical Journal International 114, 651–662. https://doi.org/10.1111/j.1365-246X.1993.tb06994.x

Westbrook, G.K., Mascle, A., Biju-Duval, B., 1984. Geophysics and the structure of the Lesser Antilles Forearc. Initial Reports Deep Sea Drilling Program, LXXVIIIA 23–38.

Wilson, D.S., 1984. Paleomagnetic results from Deep Sea Drilling Project Leg 78A. Init. Repts DSDP 78, 583 –591.

Wright, A., 1984. Sediment accumulation rates of the Lesser Antilles intraoceanic island arc, Deep Sea Drilling Project leg 78A. Init. Repts DSDP 78, 583 –591.

or other pass-through paleomagnetic data: TECHNICAL BRIEF. Geochemistry, Geophysics, Geosystems 10. https://doi.org/10.1029/2009GC002584

Xuan, C., Channell, J.E.T., Hodell, D.A., 2016. Quaternary magnetic and oxygen isotope stratigraphy in diatom-rich sediments of the southern Gardar Drift (IODP Site U1304, North Atlantic). Quaternary Science Reviews 142, 74–89. https://doi.org/10.1016/j.quascirev.2016.04.010

Yamazaki, T., Oda, H., 2005. A geomagnetic paleointensity stack between 0.8 and 3.0 Ma from equatorial Pacific sediment cores: PALEOINTENSITY STACK. Geochemistry, Geophysics, Geosystems 6. https://doi.org/10.1029/2005GC001001

Ziegler, L.B., Constable, C.G., Johnson, C.L., Tauxe, L., 2011. PADM2M: a penalized maximum likelihood model of the 0-2 Ma palaeomagnetic axial dipole moment: PADM2M revised. Geophysical Journal International 184, 1069–1089. https://doi.org/10.1111/j.1365-246X.2010.04905.x

710 Fig. 1. Bathymetric map of the middle Lesser Antilles Arc, western Atlantic Ocean using GEBCO and
711 CASEIS data. Red and yellow lines highlight, respectively, continental slope canyons and forearc
712 basin canyons. The local minimum gravity anomaly limit (black dotted line), the N 294°E strike
713 of the Tiburon ridge (dashed black lines) and the deformation front (white dashed line with teeth)
714 are derived from Bouysse and Wastercamp (1990). The location of reference core CAS16-24PC
715 is indicated in purple.

716 Fig. 2. A: Full core high-resolution photography with CT-scan images (left: TOP of the core, right:
717 BOTTOM of the core). B: MSCL and XRF data comprising from left to right: P-wave velocity,
718 density, magnetic susceptibility k, L*, CT-number, and ln (Fe/Ca). The shipboard grain size log
719 is also plotted on the right, including red marks that are pure hemipelagic background sediments
720 used to delimit the background signal with ±2σ (whitened band between red straight lines. RDL
721 are highlighted as grey horizontal intervals.

722 Fig. 3. A: Brownish hemipelagic background sediments defined with low and stable magnetic
723 susceptibility (k), CT-number, density and P-wave velocity, interbedded with a RDL (≈5 cm)
724 between 2.70 m and 2.65 m (yellow band). B: Light brown hemipelagic background sediments
725 are defined by low and stable k, CT-number, density and P-wave velocity data. A well-defined
726 RDL between 6.24 m and 6.14 m is darker (dark brown to gray color) with an erosive contact,
727 normal grading (high CT-number, P-wave velocity, density) and high k.

728 Fig. 4. SEM images for representative bulk sample VIII-1137. The left-hand image is a general view
729 of the sample. The right-hand image is focused on small particles (< 10 µm) and matrix analysis.
730 Blue bands are 10 µm scales. Red objects are elemental analyses, as referenced in Table S1 with
731 the same numbers.

loops are shown in red. B: Magnetic susceptibility vs. high temperatures. Red curves for heating, while blue curves are for cooling.

Fig. 6. A: Day plot (Day et al., 1977). Red labeled dots are data for the samples presented in figure 5. B: King plot (King et al., 1982).

Fig. 7. Magnetic properties of the pelagic sediments (event-free composite record) with concentration, and magnetic grain size-dependent parameters on the left (NRM20 mT, ARM20 mT and IRM20 mT). k_{ARM}/k indicates magnetic grain size variations for a magnetic assemblage dominated by magnetite.

Fig. 8. Paleomagnetic data including from left to right: ChRM10-40 mT, ARM, IRM and SIRM demagnetization steps. Inclination (red line is the ±GAD inclination at the site latitude) and declination (blue dots are data for the discrete samples). MAD values > 15° are indicated in dark red and > 20° in red.

Fig. 9. Typical demagnetization curves and orthogonal projections of hemipelagic sediments. Filled blue dots represent the range of demagnetization steps used to calculate the characteristic remanent magnetisation (ChRM).

Fig. 10. Comparison of the RPI estimated with the average ratios (superposed red and green curves) and slope methods (red and green curves) in the scatter plots on the left, the correlation is reduced for ARM. Demagnetization curves for NRM, ARM and IRM are presented on the right-hand side.

Fig. 11. Planktic foraminiferal $\delta^{18}O$ record for core CAS16-24PC (red curve) correlated to the LR04 benthic stack in blue (Lisiecki and Raymo, 2005). Black crosses represents the tie-points determined using the AnalySeries software (Paillard et al. 1996).

2009) in black. Upper middle: RPI record for core 24PC ratio-method normalized by ARM in red. Lower middle: paleomagnetic axial dipole moment (PADM2M) model (Ziegler et al. 2011) in grey. Notable tie-points are indicated with green dots (I-1 to I-18) and blue dots (P-1 to P-16). Bottom: compilation of PISO-1500, PADM2M and RPI record (colors are the same as above with the violet curve derived from the developed slope method).

Fig. 13. Age-depth model developed using the R package Bacon 2.2 (Blaauw and Christen, 2011) with linear interpolation using 3 paleomagnetic reversals (grey dots) and 37 tie-points (blue and green dots) from RPI (see Fig. 12) and 37 tie-points (red dots) from $\delta^{18}O$ stratigraphy (see Fig. 11). Age-errors used for each tie point correspond to half the distance samples (see Fig. S-1). Sedimentation rates are derived from the age-depth model, including RDL (gray dotted lines). B = Brunhes Chron, M = Matuyama Chron, J = Jaramillo Subchron.

Fig. 14. Planktic foraminiferal $\delta^{18}O$ record for core CAS16-24PC (blue curve) and RPI record (red curve) using the age-depth model developed in this study (Fig. 13) compared with the LR04 benthic (upper black curve), PISO-1500 (lower black curve) and PADM2M (grey curve) stacks. Odd-numbered MIS are highlighted with grey bands. B = Brunhes Chron, M = Matuyama Chron, J = Jaramillo Subchron.

Table 1. List of $\delta^{18}O$ tie points with isotopic composition of the sample and the corresponding LR04 point with age, including the error used in the age-depth model.

Table 2. List of RPI tie points determined against PISO-1500 (I1-18) and against PADM2M (P1-16), including the error used in the age-depth model.

778 Figure S-1. Schematic explanation of age-error used for the age-depth model. The half-time gap
779 between a tie-point and its surrounding values is represented in green and purple segments. The
780 longest half-time gap (green segments) is set as this specific tie-point age-error.

781 Figure S-2. Inclination, declination and relative paleointensity records for core CAS16-24PC.

782 Table S-1: Meter composite depth (MCD) correspondence with original coring depth in meters.

783 Table S-2. Major elemental percentages obtained by energy dispersive X-ray spectroscopy (EDS) in
784 samples indicated in Fig. 4.

Composite depth (m)	$\delta^{18}O_{planktic}$ (‰)	Age (ka)	LR04 $\delta^{18}O_{benthic}$ (‰)	Error (± ka)
0.05	-1.84	4	3.3	3.75
0.9	-0.41	60	4.60	2.5
1.87	-1.72	124	3.27	2.5
2.34	0.25	139	4.87	5
2.95	-0.76	188	4.46	7
3.15	-1.45	203	3.61	4
3.65	-0.95	229	4.02	5
3.85	-1.16	240	3.44	5
4.27	-1.1	285	3.84	4.5
4.67	-1.05	296	4.23	5
4.87	-1.28	317	3.89	5
5.07	-1.74	326	3.23	3
5.37	-0.28	343	4.8	3.5
5.98	-1.18	384	4.08	3.5
6.28	-1.6	405	3.11	4.5
7.13	-0.49	476	4.3	3.5
7.49	-1.31	491	3.47	4.5
7.79	-0.82	510	4.14	3.5
7.94	-0.98	525	3.92	11
8.14	-0.52	547	4.53	11
8.8	-1.66	579	3.57	7
9.42	-1.74	614	3.53	3.5
9.72	-0.2	634	4.93	3.5
10.29	-0.44	676	4.4	3.5
10.99	-1.34	696	3.5	4
11.26	-0.29	720	4.66	4
11.7	-0.79	740	4.11	2.5
11.94	-0.31	756	4.59	4
12.23	-1.31	780	3.48	4
12.81	-1.38	822	3.9	6.5
13.11	-1.37	860	3.45	6.5
14.46	-2.12	954	3.39	3
15.7	-1.17	1022	3.94	3
16.31	-1.41	1068	3.66	8
16.90	-0.68	1126	4.5	4
17.26	-1.51	1148	4.02	9

Table 1. List of $\delta^{18}O$ tie points with isotopic composition of the sample and the corresponding LR04 point with age, including the error used in the age-depth model.

Composite depth (m)	RPI	Age (ka)	Models (10^{22} Am^2)	Error (± ka)
0.36 P-1	0.94	20	4.59	2
0.51 P-2	1.52	23	6.01	2
0.68 P-3	1.13	41	3.48	2
1.11 P-4	0.78	65	5.07	2
1.34 I-1	1.26	92	9.62	1
1.41 I-2	0.83	99	3.59	1
2.14 P-5	2.01	139	7.10	2
2.85 P-6	2.23	169	7.10	2
3.07 I-3	0.46	194	2.34	2
3.28 P-7	1.05	203	6.32	1
3.28 I-4	1.05	205	9.24	1
3.63 P-8	1.07	219	5.52	2
3.72 I-5	1.62	231	13.11	1
3.88 P-9	1.10	242	5.16	2
4.43 P-10	0.50	294	4.25	1
5.52 I-6	2.45	348	13.51	2
6.07 I-7	0.68	394	10.81	1
6.44 I-8	1.51	415	11.04	2
7.85 I-9	1.92	510	10.46	2
8.70 I-10	2.16	569	12.34	1
9.12 P-11	0.50	596	4.69	1
9.53 P-12	0.53	617	5.14	2
10.33 P-13	1.59	667	8.21	1
10.55 I-11	0.48	685	3.97	1
11.19 P-14	0.73	712	5.55	1
11.38 I-12	1.83	723	9.48	1
12.24 I-13	0.36	771	1.41	2
13.47 I-14	1.72	871	8.06	1
13.60 I-15	0.58	890	2.62	2
13.87 I-16	2.70	901	7.68	1
14.44 I-17	0.13	936	2.30	2
14.75 I-18	0.88	961	10.32	1
15.48 I-19	0.87	1001	11.27	2
16.01 I-20	0.94	1062	13.21	1
16.33 I-21	0.08	1071	1.05	2
16.57 P-15	1.07	1106	4.76	1
16.74 P-16	0.38	1122	2.92	2

Table 2. List of RPI tie points determined against PISO-1500 (I1-18) and against PADM2M (P1-16), including the error used in the age-depth model.

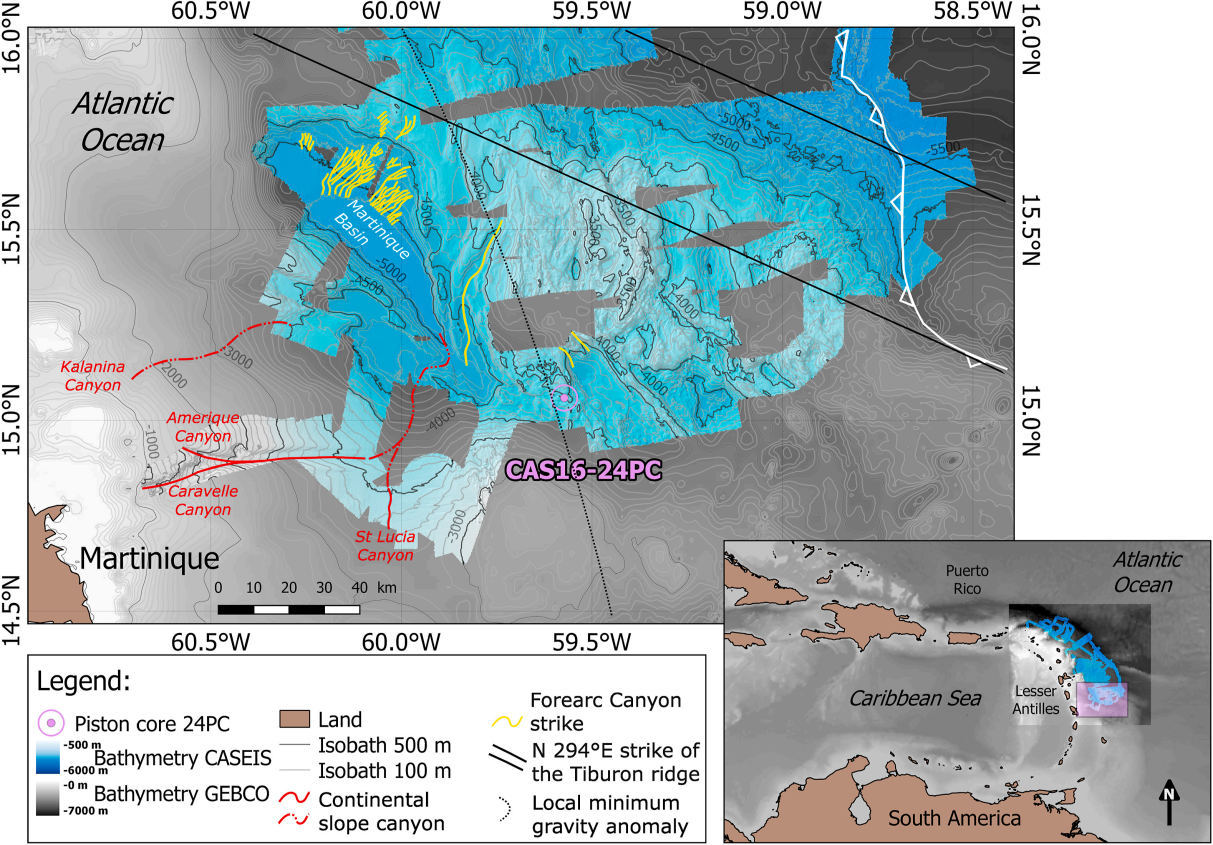
60.5°W
60.0°W
59.5°W
59.0°W
58.5°W
16.0°N
15.5°N
15.0°N
14.5°N
Atlantic Ocean
Martinique Basin
Kalanina Canyon
Amerique Canyon
Caravelle Canyon
St Lucia Canyon
CAS16-24PC
Martinique
0 10 20 30 40 km
Legend:
Piston core 24PC
-500 m
-6000 m
Bathymetry CASEIS
-0 m
-7000 m
Bathymetry GEBCO
Land
Isobath 500 m
Isobath 100 m
Continental slope canyon
Forearc Canyon strike
N 294°E strike of the Tiburon ridge
Local minimum gravity anomaly
Puerto Rico
Atlantic Ocean
Caribbean Sea
Lesser Antilles
South America
N

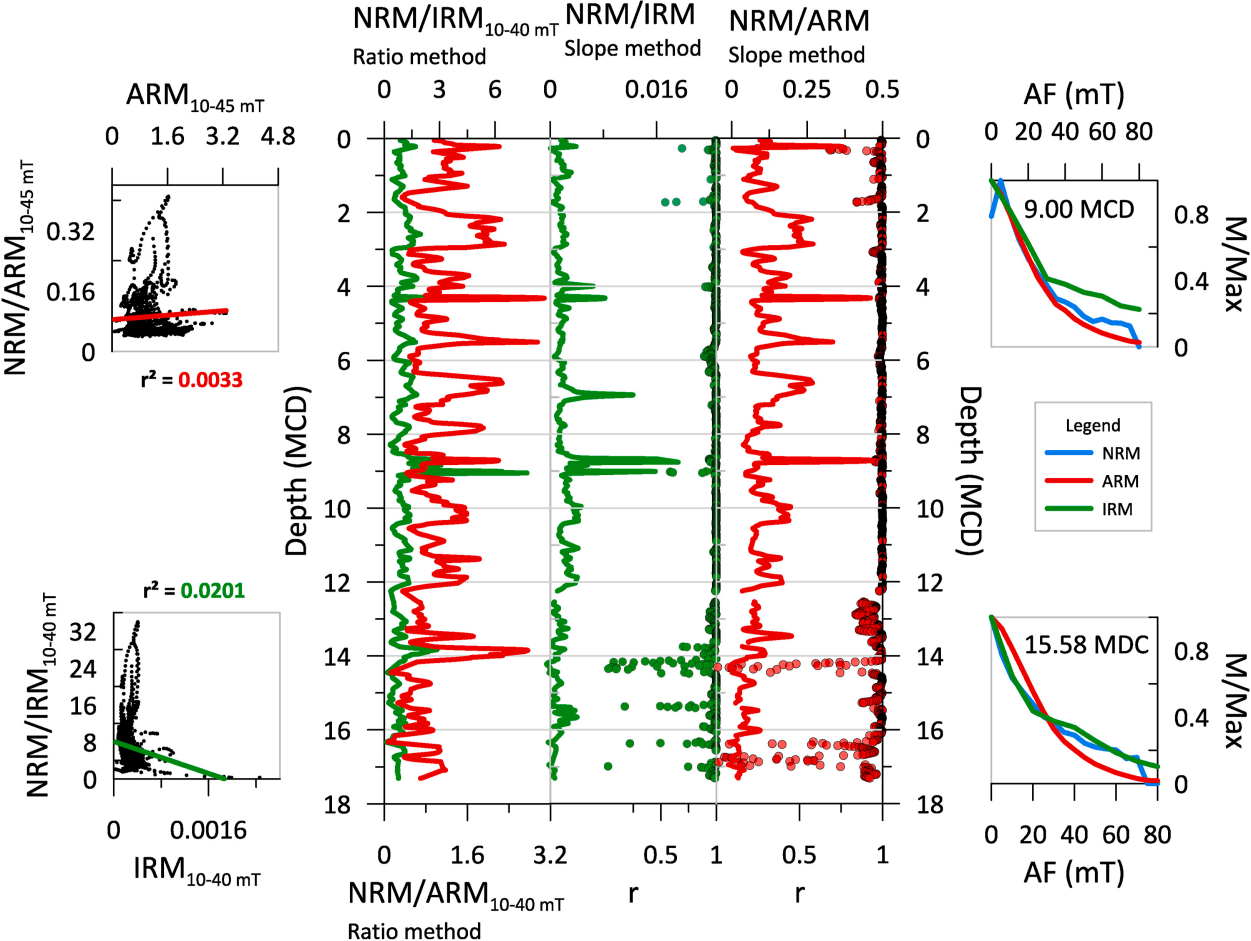
NRM/IRM10-40 mT
Ratio method
NRM/IRM
Slope method
NRM/ARM
Slope method
ARM10-45 mT
AF (mT)
9.00 MCD
15.58 MDC
NRM/ARM10-45 mT
r² = 0.0033
r² = 0.0201
NRM/IRM10-40 mT
IRM10-40 mT
Depth (MCD)
Legend
NRM
ARM
IRM
M/Max
NRM/ARM10-40 mT
Ratio method
r
r

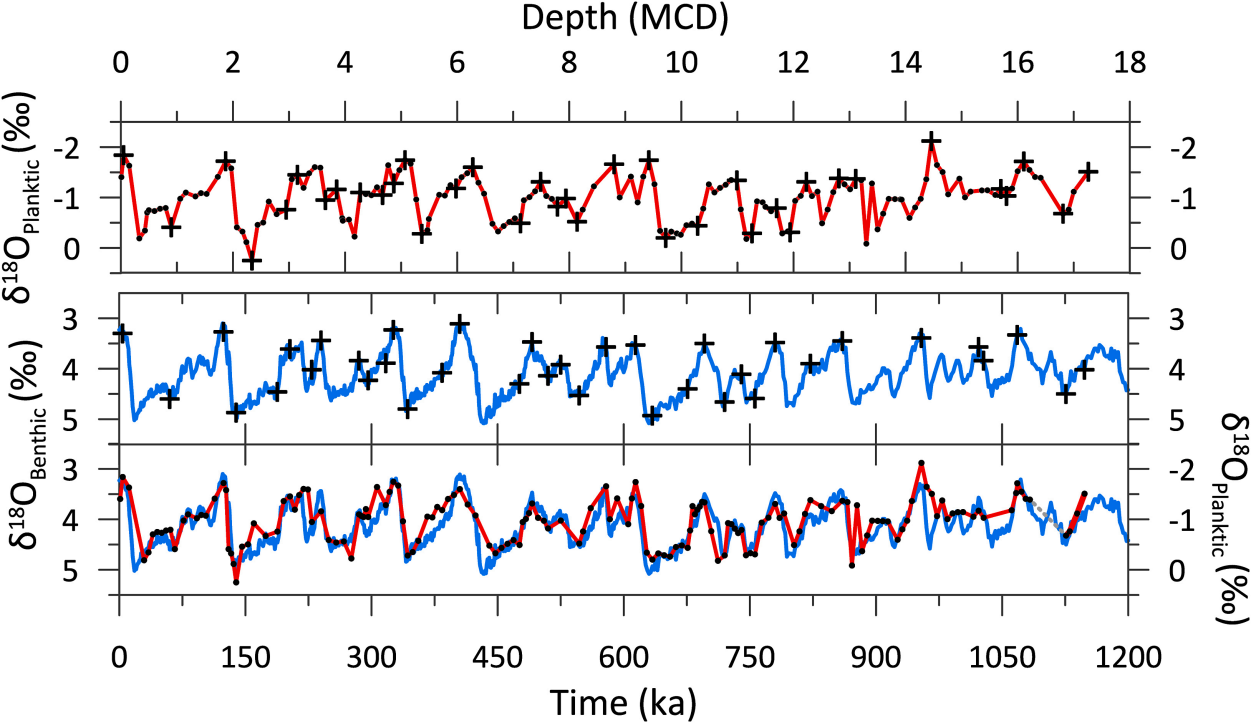
Depth (MCD)
0
2
4
6
8
10
12
14
16
18
δ18OPlanktic (‰)
-2
-1
0
δ18OBenthic (‰)
3
4
5
δ18OBenthic (‰)
3
4
5
δ18OPlanktic (‰)
-2
-1
0
0
150
300
450
600
750
900
1050
1200
Time (ka)

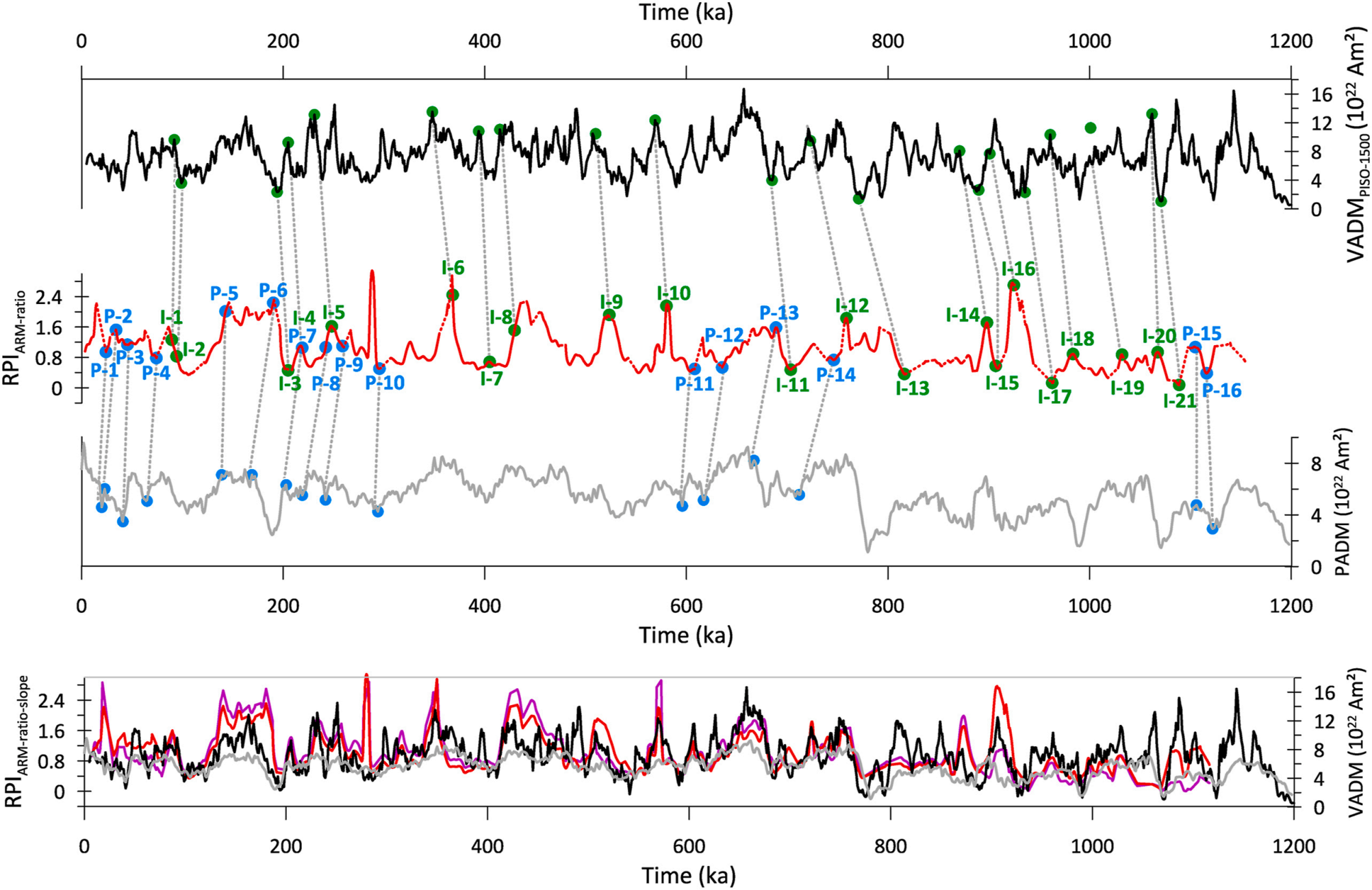
Time (ka)
0
200
400
600
800
1000
1200
VADM$_{PISO-1500}$ (10^{22} Am^2)
16
12
8
4
0
RPI$_{ARM-ratio}$
2.4
1.6
0.8
0
I-1
I-2
I-3
I-4
I-5
I-6
I-7
I-8
I-9
I-10
I-11
I-12
I-13
I-14
I-15
I-16
I-17
I-18
I-19
I-20
I-21
P-1
P-2
P-3
P-4
P-5
P-6
P-7
P-8
P-9
P-10
P-11
P-12
P-13
P-14
P-15
P-16
PADM (10^{22} Am^2)
8
4
0
Time (ka)
RPI$_{ARM-ratio-slope}$
2.4
1.6
0.8
0
VADM (10^{22} Am^2)
16
12
8
4
0
Time (ka)

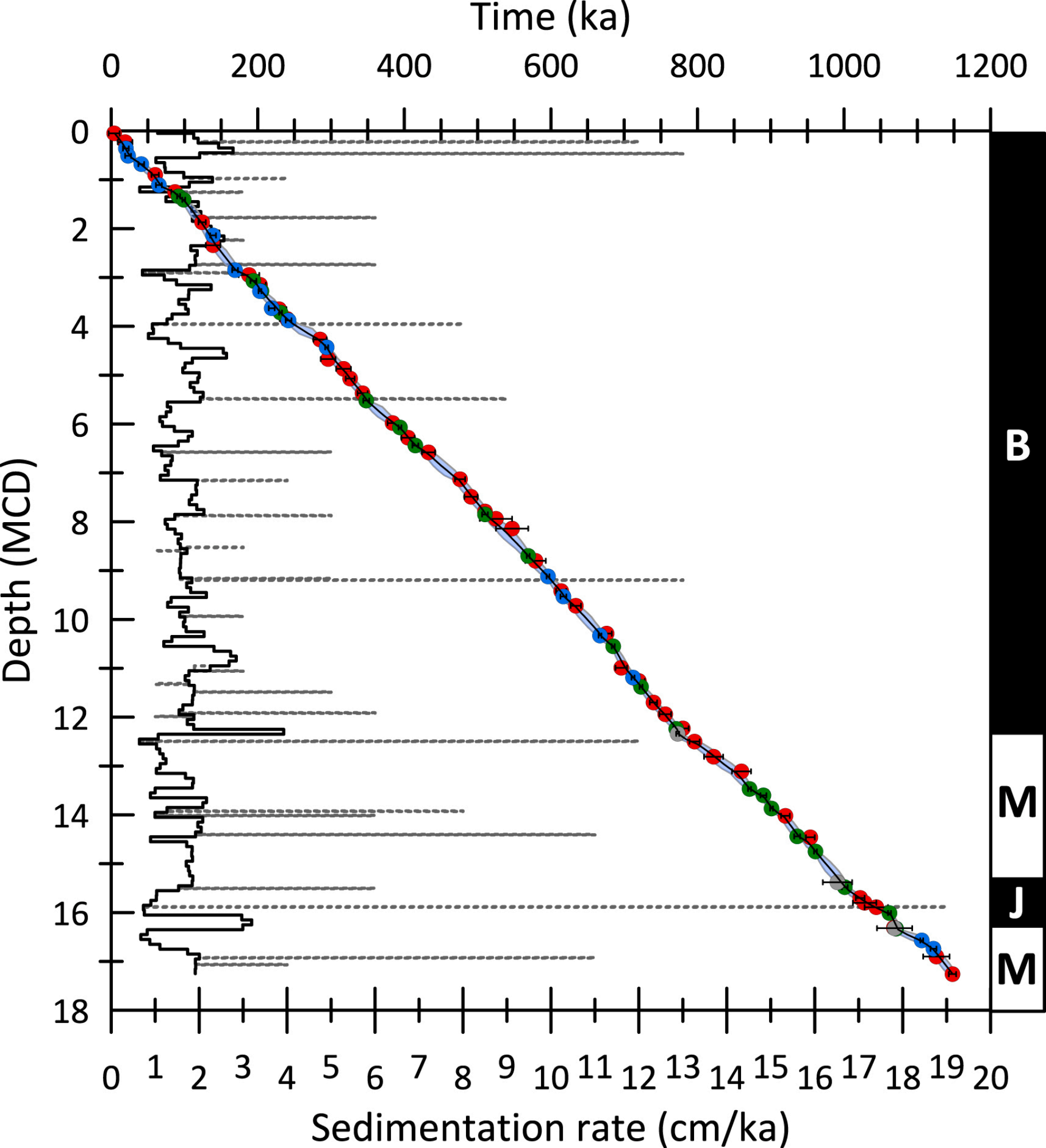
Time (ka)
0
200
400
600
800
1000
1200
Depth (MCD)
0
2
4
6
8
10
12
14
16
18
B
M
J
M
0
1
2
3
4
5
6
7
8
9
10
11
12
13
14
15
16
17
18
19
20
Sedimentation rate (cm/ka)

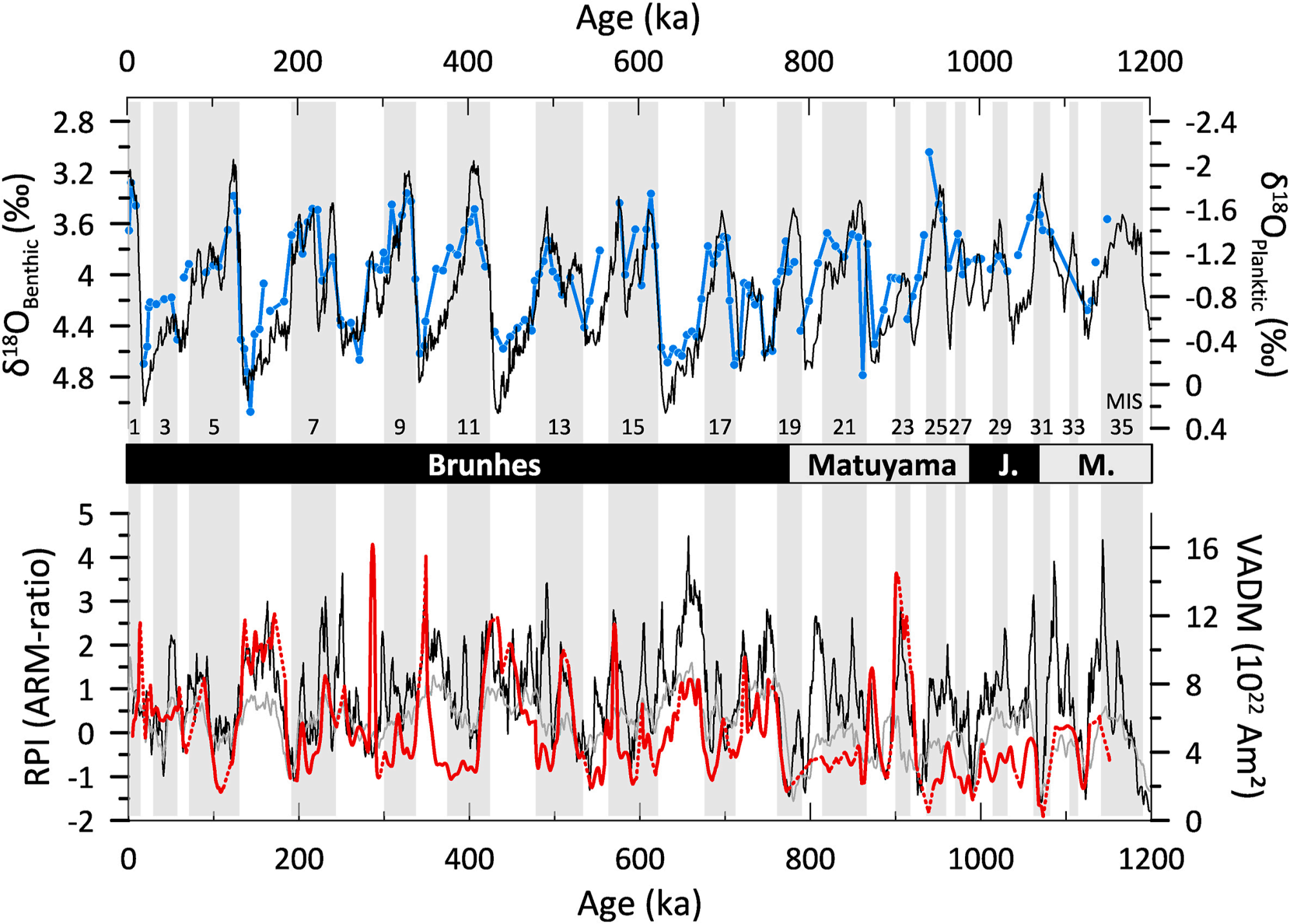
Age (ka)
0
200
400
600
800
1000
1200
δ18OBenthic (‰)
2.8
3.2
3.6
4
4.4
4.8
δ18OPlanktic (‰)
-2.4
-2
-1.6
-1.2
-0.8
-0.4
0
0.4
MIS
1 3 5 7 9 11 13 15 17 19 21 23 25 27 29 31 33 35
Brunhes
Matuyama
J.
M.
RPI (ARM-ratio)
5
4
3
2
1
0
-1
-2
VADM (10²² Am²)
16
12
8
4
0
Age (ka)

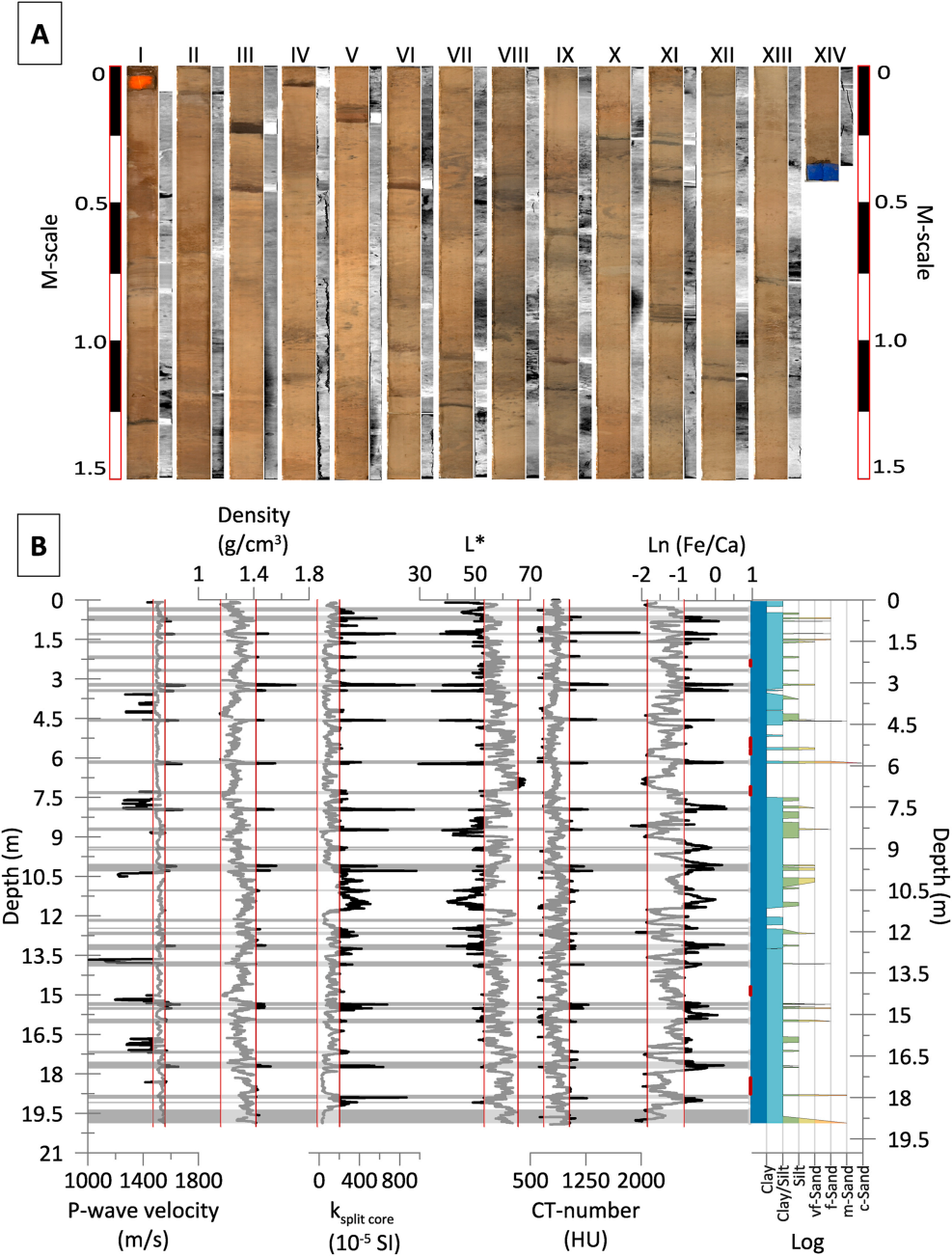
A
I
II
III
IV
V
VI
VII
VIII
IX
X
XI
XII
XIII
XIV
0
0.5
1.0
1.5
M-scale
B
Density
(g/cm³)
1
1.4
1.8
L*
30
50
70
Ln (Fe/Ca)
-2
-1
0
1
Depth (m)
0
1.5
3
4.5
6
7.5
9
10.5
12
13.5
15
16.5
18
19.5
21
1000 1400 1800
P-wave velocity
(m/s)
0 400 800
k split core
(10-5 SI)
500 1250 2000
CT-number
(HU)
Clay
Clay/Silt
Silt
vf-Sand
f-Sand
m-Sand
c-Sand
Log

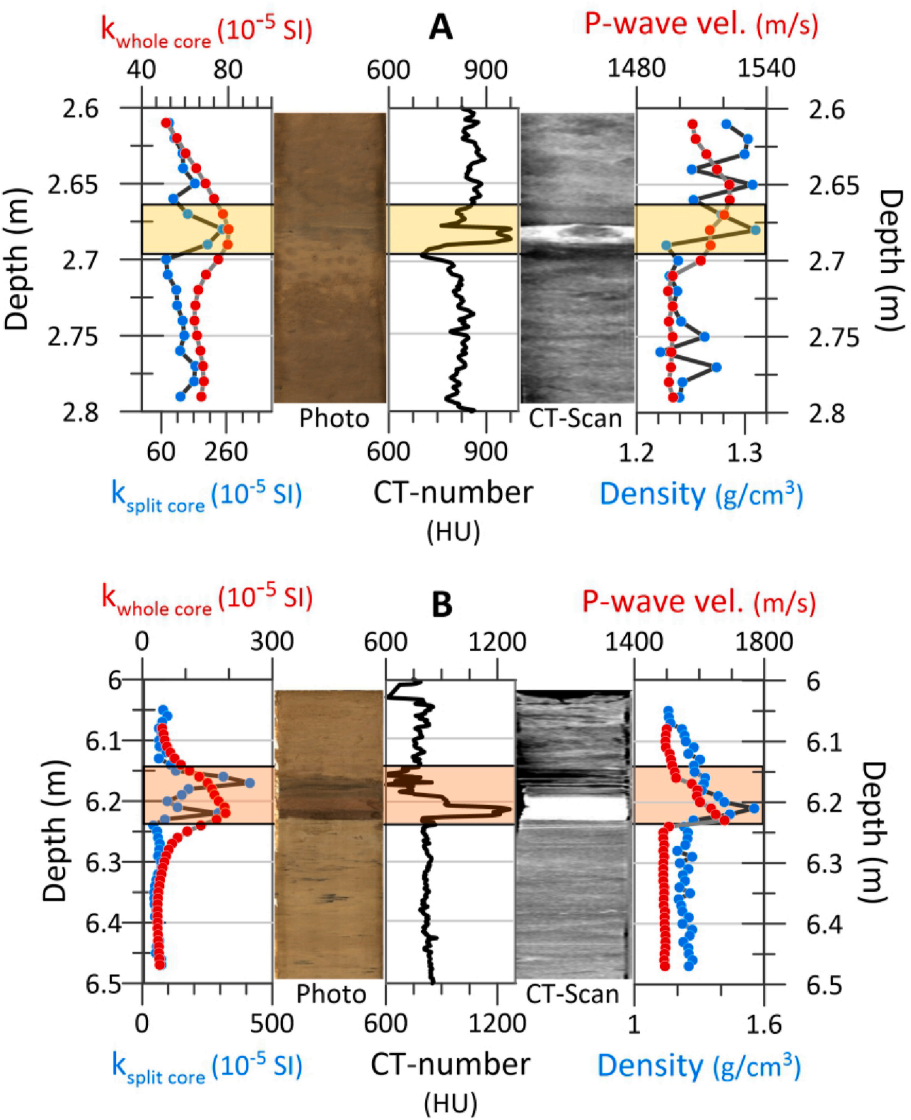
A
$k_{whole\ core}$ (10^{-5} SI)
P-wave vel. (m/s)
40
80
600
900
1480
1540
2.6
2.65
2.7
2.75
2.8
Depth (m)
Photo
CT-Scan
60
260
600
900
1.2
1.3
$k_{split\ core}$ (10^{-5} SI)
CT-number (HU)
Density (g/cm^3)
B
$k_{whole\ core}$ (10^{-5} SI)
P-wave vel. (m/s)
0
300
600
1200
1400
1800
6
6.1
6.2
6.3
6.4
6.5
Depth (m)
Photo
CT-Scan
0
500
600
1200
1
1.6
$k_{split\ core}$ (10^{-5} SI)
CT-number (HU)
Density (g/cm^3)

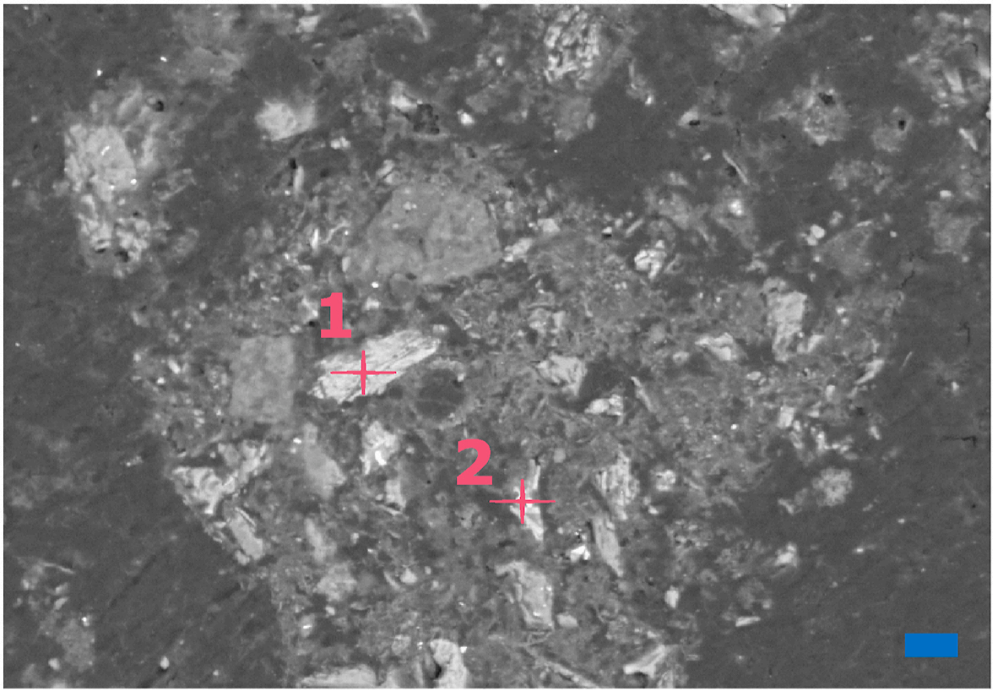
1
2

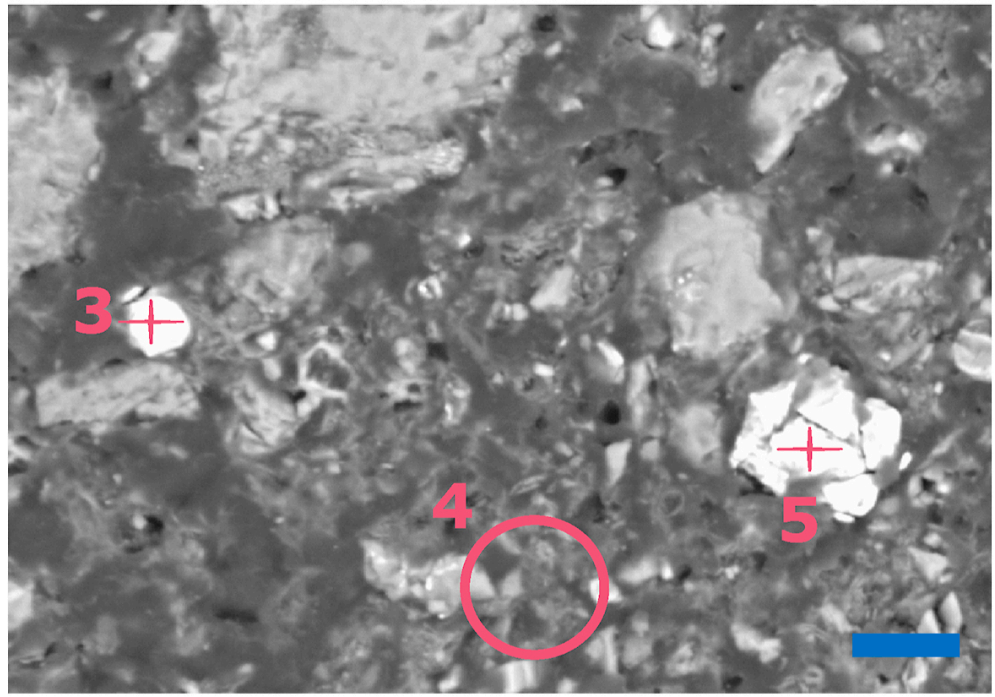
3
4
5

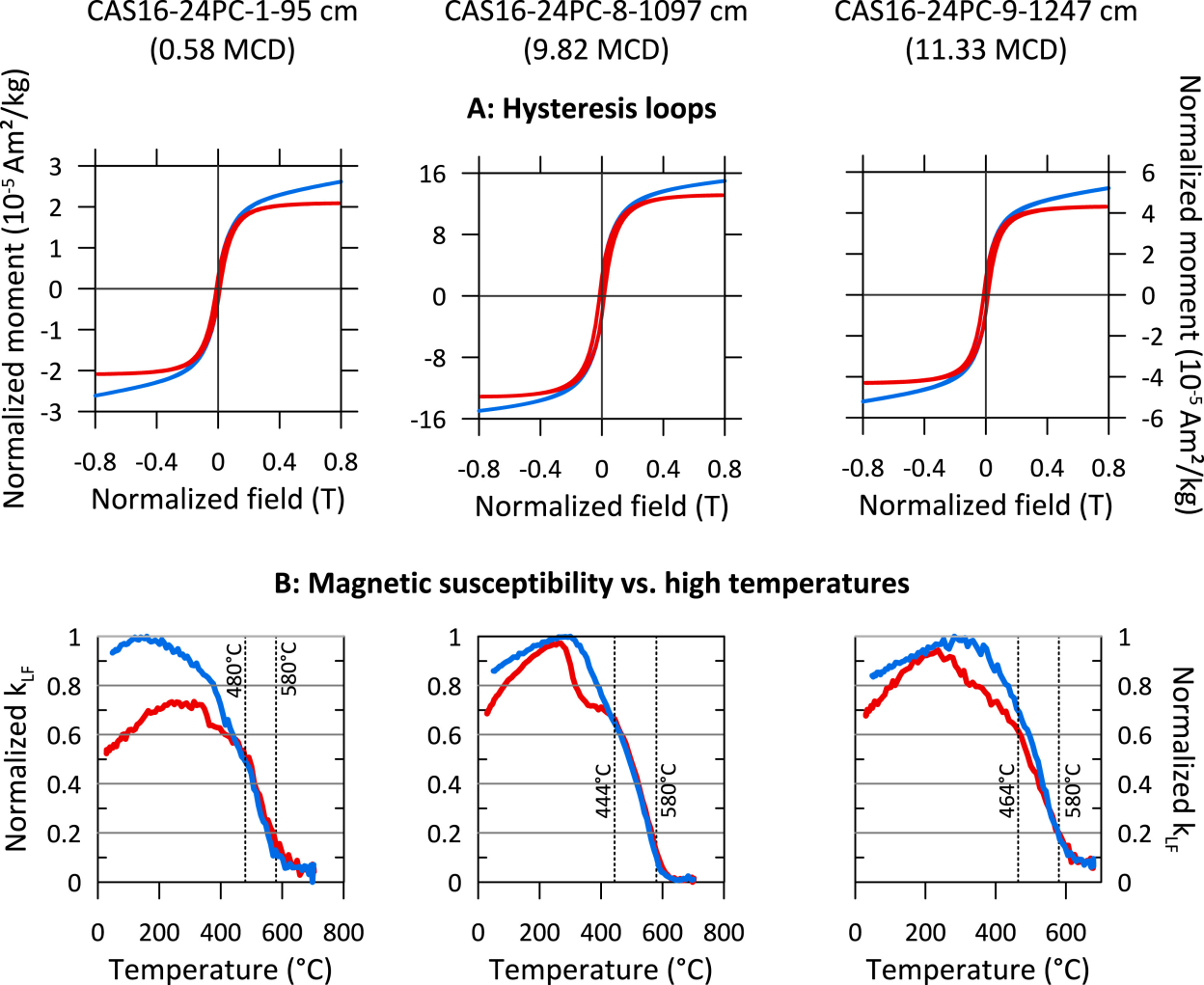
CAS16-24PC-1-95 cm
(0.58 MCD)
CAS16-24PC-8-1097 cm
(9.82 MCD)
CAS16-24PC-9-1247 cm
(11.33 MCD)
A: Hysteresis loops
Normalized moment (10-5 Am2/kg)
Normalized field (T)
B: Magnetic susceptibility vs. high temperatures
Normalized kLF
480°C
580°C
444°C
580°C
464°C
580°C
Temperature (°C)

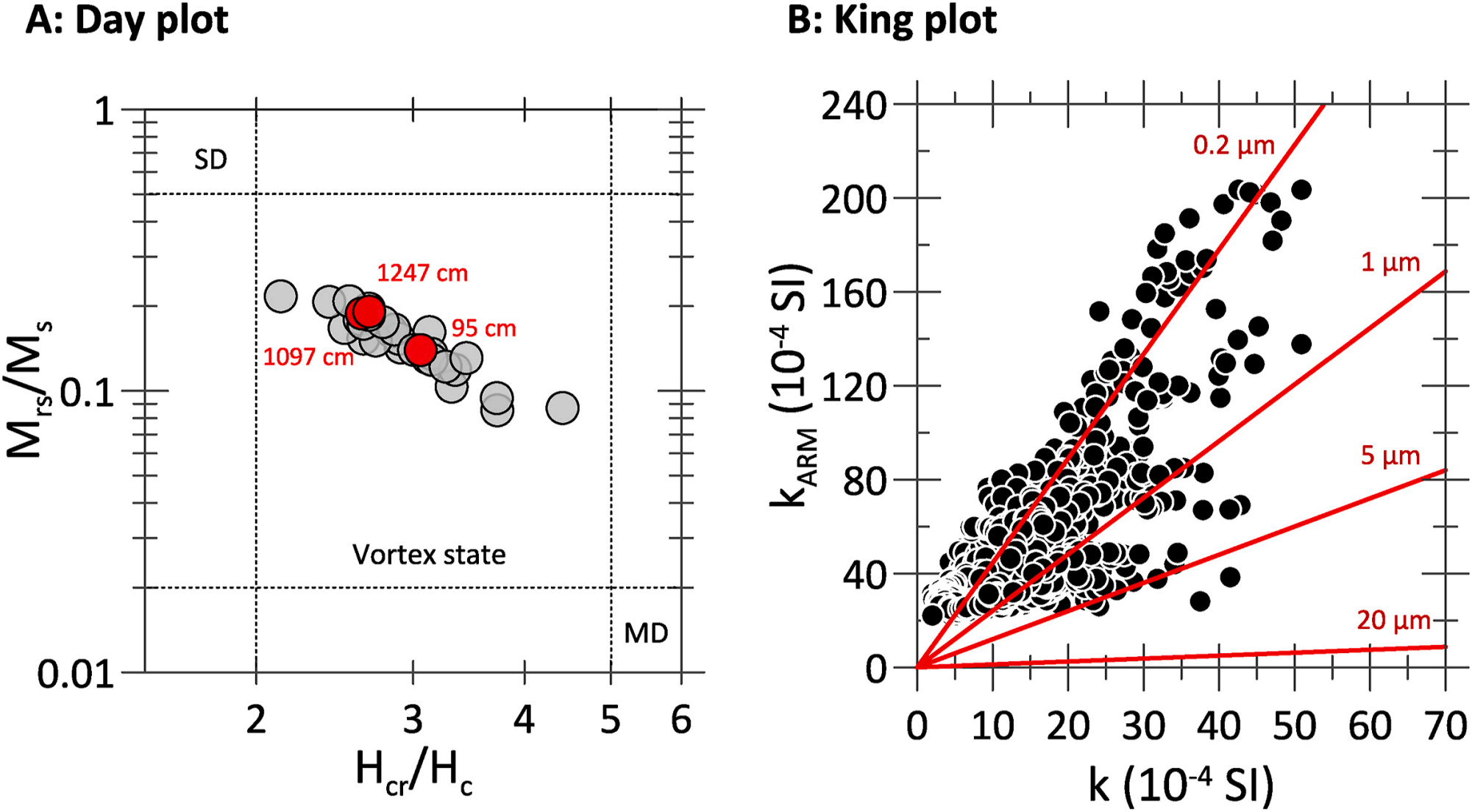
A: Day plot
B: King plot
SD
Vortex state
MD
1247 cm
95 cm
1097 cm
1
0.1
0.01
2
3
4
5
6
M_{rs}/M_s
H_{cr}/H_c
0.2 µm
1 µm
5 µm
20 µm
240
200
160
120
80
40
0
0
10
20
30
40
50
60
70
k_{ARM} (10^{-4} SI)
k (10^{-4} SI)

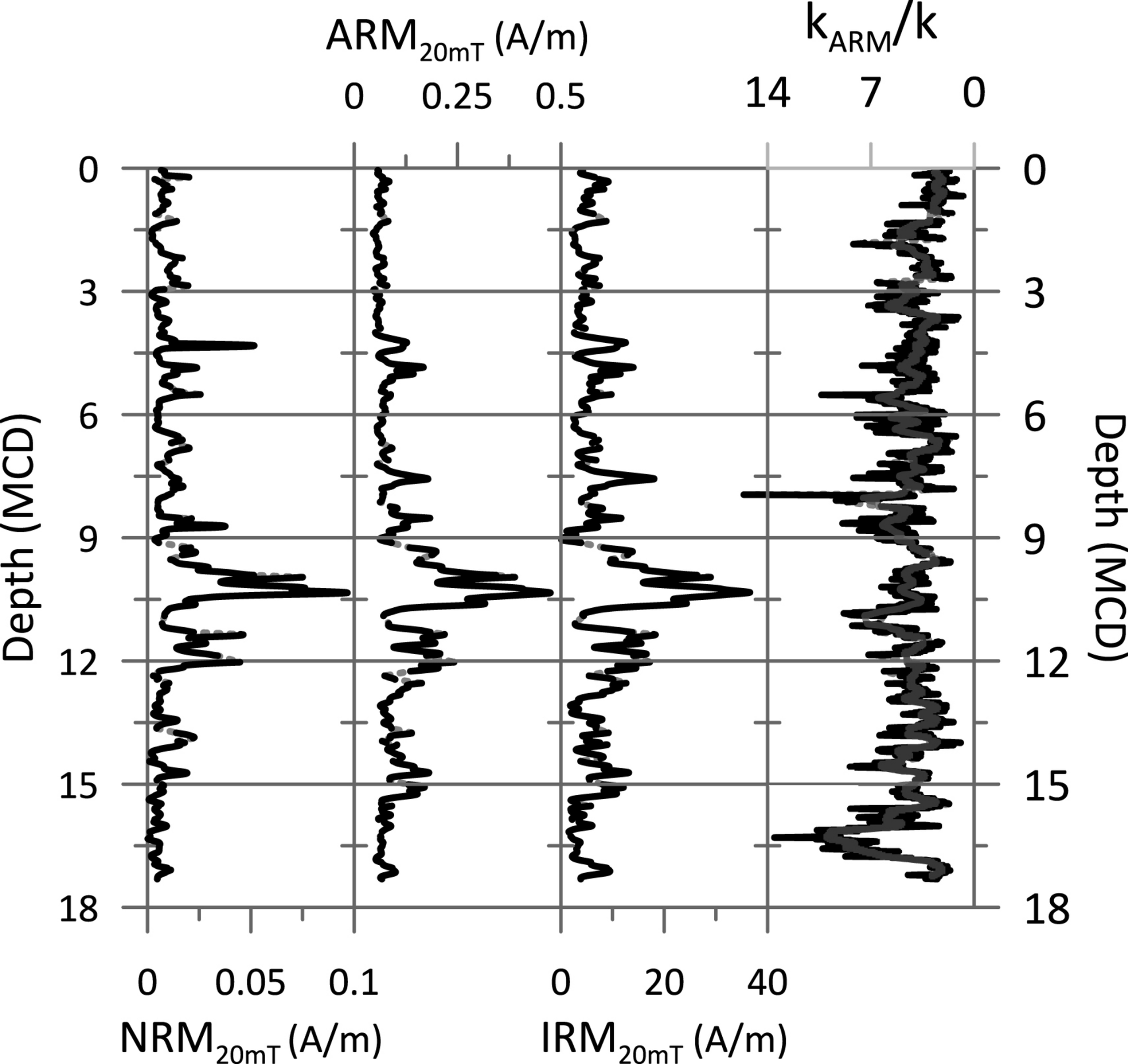
ARM20mT (A/m)
0
0.25
0.5
kARM/k
14
7
0
Depth (MCD)
0
3
6
9
12
15
18
0
0.05
0.1
NRM20mT (A/m)
0
20
40
IRM20mT (A/m)

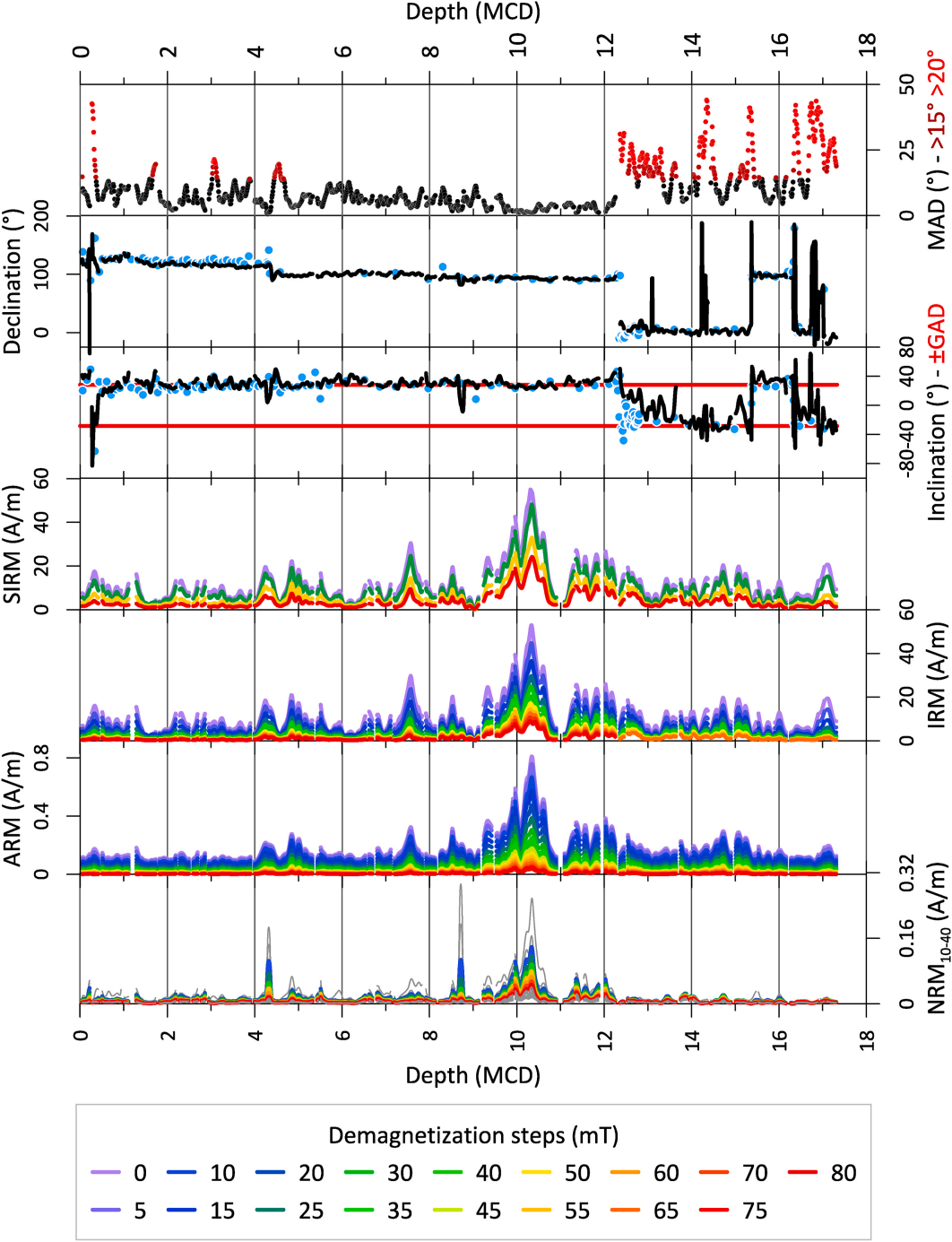
Depth (MCD)
0
2
4
6
8
10
12
14
16
18
Declination (°)
0
100
200
MAD (°) - >15° >20°
0
25
50
Inclination (°) - ±GAD
-80
-40
0
40
80
SIRM (A/m)
0
20
40
60
IRM (A/m)
0
20
40
60
ARM (A/m)
0
0.4
0.8
NRM10-40 (A/m)
0
0.16
0.32
Depth (MCD)
Demagnetization steps (mT)
0
5
10
15
20
25
30
35
40
45
50
55
60
65
70
75
80

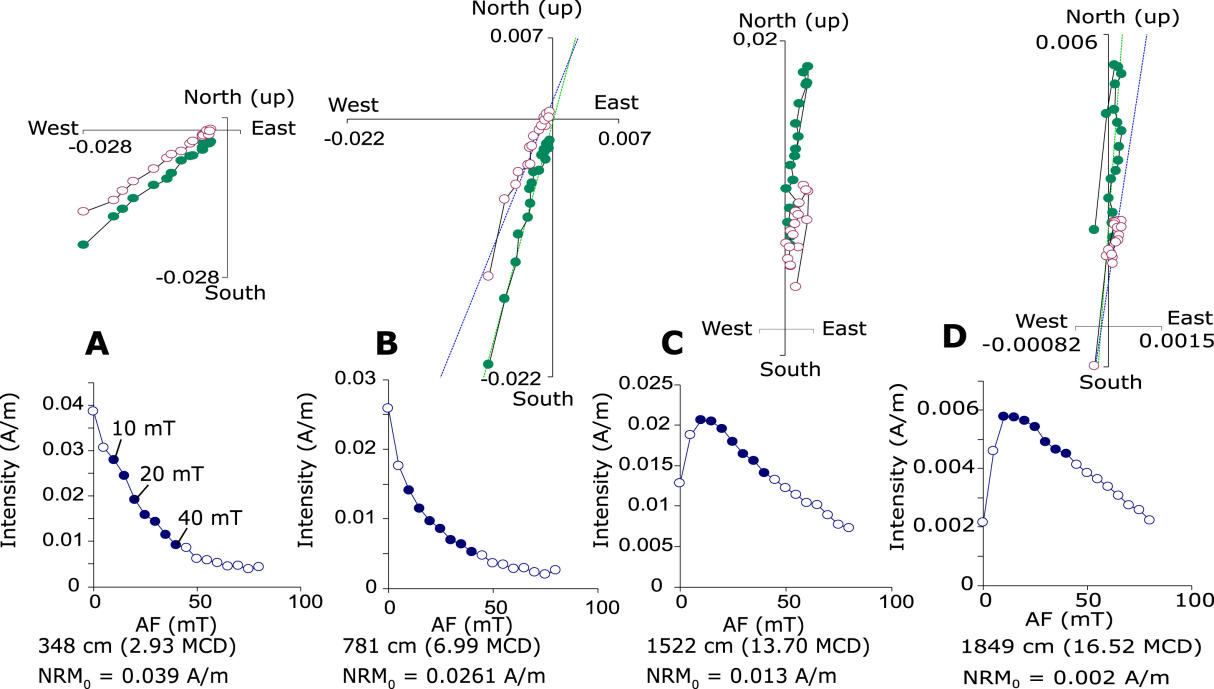
North (up)
West
East
-0.028
-0.028
South
A
10 mT
20 mT
40 mT
Intensity (A/m)
AF (mT)
348 cm (2.93 MCD)
NRM0 = 0.039 A/m
North (up)
0.007
West
East
-0.022
0.007
-0.022
South
B
Intensity (A/m)
AF (mT)
781 cm (6.99 MCD)
NRM0 = 0.0261 A/m
North (up)
0,02
West
East
South
C
Intensity (A/m)
AF (mT)
1522 cm (13.70 MCD)
NRM0 = 0.013 A/m
North (up)
0.006
West
East
-0.00082
0.0015
South
D
Intensity (A/m)
AF (mT)
1849 cm (16.52 MCD)
NRM0 = 0.002 A/m

Declaration of interests

☒ The authors declare that they have no known competing financial interests or personal relationships that could have appeared to influence the work reported in this paper.

☐The authors declare the following financial interests/personal relationships which may be considered as potential competing interests: